Bioinspired sandwich-like hybrid surface functionalized scaffold capable of regulating osteogenesis, angiogenesis, and osteoclastogenesis for robust bone regeneration

Minhao Wu [a,1], Feixiang Chen [b,1], Huifan Liu [a,1], Ping Wu [c], Zhiqiang Yang [a], Zhe Zhang [d], Jiajia Su [e,***], Lin Cai [a,**], Yufeng Zhang [a,*]

[a] Department of Spine Surgery and Musculoskeletal Tumor, Zhongnan Hospital of Wuhan University, 168 Donghu Street, Wuchang District, Wuhan, 430071, Hubei, China
[b] Department of Biomedical Engineering and Hubei Province Key Laboratory of Allergy and Immune Related Diseases, School of Basic Medical Sciences, Wuhan University, Wuhan, 430071, China
[c] College of Life Science and Technology Huazhong University of Science and Technology, Wuhan, 430074, China
[d] National Demonstration Center for Experimental General Medicine Education, Xianning Medical College, Hubei University of Science and Technology, China
[e] Department of Radiology, Hubei Cancer Hospital, Tongji Medical College, Huazhong University of Science and Technology, Wuhan, China

ARTICLE INFO

ABSTRACT

Recently, strategies that focus on biofunctionalized implant surfaces to enhance bone defect healing through the synergistic regulation of osteogenesis, angiogenesis, and osteoclastogenesis have attracted increasing attention in the bone tissue engineering field. Studies have shown that the Wnt/β-catenin signaling pathway has an imperative effect of promoting osteogenesis and angiogenesis while reducing osteoclastogenesis. However, how to prepare biofunctionalized bone implants with balanced osteogenesis, angiogenesis, and osteoclastogenesis by activating the Wnt/β-catenin pathway has seldom been investigated. Herein, through a bioinspired dopamine chemistry and self-assembly method, BML-284 (BML), a potent and highly selective Wnt signaling activator, was loaded on a mussel-inspired polydopamine (PDA) layer that had been immobilized on the porous beta-tricalcium calcium phosphate (β-TCP) scaffold surface and subsequently modified by a biocompatible carboxymethyl chitosan hydrogel to form a sandwich-like hybrid surface. β-TCP provides a biomimetic three-dimensional porous microenvironment similar to that of natural cancellous bone, and the BML-loaded sandwich-like hybrid surface endows the scaffold with multifunctional properties for potential application in bone regeneration. The results show that the sustained release of BML from the sandwich-like hybrid surface significantly facilitates the adhesion, migration, proliferation, spreading, and osteogenic differentiation of MC3T3-E1 cells as well as the angiogenic activity of human umbilical vein endothelial cells. In addition to osteogenesis and angiogenesis, the hybrid surface also exerts critical roles in suppressing osteoclastic activity. Remarkably, in a critical-sized cranial defect model, the biofunctionalized β-TCP scaffold could potentially trigger a chain of biological events: stimulating the polarization of M2 macrophages, recruiting endogenous stem cells and endothelial cells at the injury site to enable a favorable microenvironment for greatly accelerating bone ingrowth and angiogenesis while compromising osteoclastogenesis, thereby promoting bone healing. Therefore, these surface-biofunctionalized β-TCP implants, which regulate the synergies of osteogenesis, angiogenesis, and anti-osteoclastogenesis, indicate strong potential for clinical application as advanced orthopedic implants.

---

* Corresponding author.
** Corresponding author.
*** Corresponding author.
  E-mail addresses: kloselovemm@163.com (J. Su), orthopedics@whu.edu.cn (L. Cai), 743838733@qq.com (Y. Zhang).
[1] These authors contributed equally to this work.

1. Introduction

Over the past several decades, accumulating evidence has well established that bone healing entails a well-orchestrated series of biological events, including early inflammatory immune regulation, angiogenesis, osteogenesis, osteoclastogenesis, and matrix mineralization, which are regulated through multiple cellular and molecular interactions [1,2]. Accordingly, interference with any of these processes may significantly impede successful bone healing. Moreover, bone regeneration or bone defect repair involves not only mesenchymal stem cells (MSCs), osteoprogenitors, and osteoblasts but also endothelial cells (ECs), osteoclasts, and different types of immune cells, which produce both intrinsic and extrinsic inductive factors and require their coordinated activities in a hierarchical spatiotemporal model [3]. Current understanding supports that bone defect repair is achieved via proliferation and differentiation of MSCs and skeletal progenitors followed by the synthesis of extracellular matrix (ECM), while enhanced EC functionality and suitable osteoclast activity also contribute to the process [4]. For example, insufficient vascularization results in failure of bone repair, yet rebuilding blood vessels is believed to accelerate tissue healing and osteogenesis of MSCs. The timely construction of the vascular system during bone repair is conducive to sufficient nutrition exchange, progenitor cells, and circulating factor delivery [5,6]. Previous studies have demonstrated that osteogenesis and angiogenesis are tightly coupled in the process of bone regeneration [6]. Additionally, increasing evidence suggests that, in addition to enhancing osteogenesis and angiogenesis, osteogenesis without osteoclastic activity may yield undesired bone overgrowth, while an adequate reduction in osteoclastogenesis is necessary for bone remodeling [1]. Therefore, altering MSC viability, the angiogenic potential of ECs, and osteoclast differentiation have individually been reported to improve fracture repair; however, the synergistic effect of these three processes on bone defect repair has yet to be investigated.

Recent researchers are also aware of the importance of synergistically regulating angiogenesis, osteogenesis, and anti-osteoclastogenesis with slow-release bioactive components from biomaterial scaffolds [1,7,8]. Nevertheless, some studies must use a series of bioactive compounds and complex strategies to impart bone repair scaffolds with enhanced osteogenic and angiogenic potential and suitable osteoclast activity, which artificially increases the complexity of mechanistic studies [4]. Furthermore, the introduction of exogenous chemical components may result in severe cytotoxicity and reduce the biocompatibility of the biomaterial scaffold. As the most important regulators of bone, osteogenic agents (such as bone morphogenetic protein; BMP) and angiogenic agents (such as vascular endothelial growth factor; VEGF) have been approved by the Food and Drug Administration (FDA) and widely used in bone regeneration applications since they can not only improve osteoblast precursor cell differentiation into mature osteoblasts but also accelerate their early neovascularization at the site of bone injury [9,10]. However, they also possess some fatal drawbacks, including expensiveness, easy deactivation, and insufficient mineralization, which affect the progress of bone physiologic reconstruction to a large extent [11,12]. Previous studies have shown that the combined delivery of BMPs and VEGF synergistically enhances bone healing [13]. Additionally, this strategy focuses mainly on osteoinduction and the differentiation of osteoblasts as well as angiogenesis without considering the influence of osteoclastogenesis on bone healing. Therefore, it is of great value to achieve the synergistic regulation of osteogenesis, angiogenesis, and osteoclastogenesis with a relatively simple and highly effective strategy. BML-284 (BML), a potent and highly selective Wingless and int-1 (Wnt) signaling activator, has unique anti-inflammatory, antioxidative, and antitumor roles that work in a dose-dependent manner [14,15]. An increasing number of works have highlighted the importance of the Wnt signaling pathway during skeletal development as well as later in life to maintain bone mass. Transcriptional profiling and spatial gene expression analysis have demonstrated a variety of Wnt signaling molecules that are involved in the process of bone fracture healing [16]. Over the past decades, accumulated evidence has indicated that the activation of the Wnt signaling pathway is effective in enhancing bone defect healing through synergistic osteogenesis-angiogenesis regulation. Moreover, recent studies have shown that the Wnt pathway plays an indispensable role in osteoclastogenesis [17,18]. Specifically, Wnts can induce the expression of osteoprotegerin/osteoclastogenesis inhibitory factor (OPG/OCIF) on osteoblasts by modulating the differentiation of osteoclasts and influencing the function of osteoclasts, which also ultimately affects the bone resorption process [22]. Thus, the Wnt signaling pathway is capable of facilitating bone remodeling by regulating both bone resorption and bone formation processes, which enabled its targeted agonist BML to be considered a small-molecule drug candidate for functional bone regeneration. However, whether the introduction of BML in the engineered bone scaffolds could regulate osteoblast/osteoclast differentiation and vascularization, thus favoring bone defect healing, remains to be further investigated. As a small-molecule agonist of the Wnt signaling pathway, the application of BML without proper delivery systems will suffer from several limitations, including poor physiological stability, rapid release of bioactive molecules, nonspecific targeting, and low cell membrane permeability. Thus, it is highly desirable to design a new drug delivery system for realizing effective and sustained release of BML for the rapid repair of bone defects. To explore ways to solve these problems, we designed a bioinspired sandwich-like surface-functionalized beta-tricalcium calcium phosphate (β-TCP) porous composite scaffold for synergistic therapy of large bone defects through the regulation of osteogenesis, angiogenesis, and osteoclastogenesis. BML-loaded hybrid films on β-TCP substrates were prepared by bioinspired dopamine chemistry and self-assembly methods. In general, loading should be performed under mild conditions when combining BML with a bone repair scaffold to maintain the bioactivity of BML. Physical adsorption can be utilized because it is simple and requires no chemical grafting reagents, altering the BML structure. However, conventional physical adsorption cannot realize a high loading efficiency and slow BML release. Inspired by marine mussel adhesion phenomena in nature, previous studies showed that the polydopamine (PDA)-assisted immobilization strategy was an attractive tool for high-efficiency drug loading. Various peptides, growth factors, or other small molecules can be incorporated into porous scaffolds via PDA deposition to enhance the regenerative capacity for bone regeneration applications [19–21]. Thus, a mussel-inspired strategy via PDA achieves excellent drug loading and sustained drug release compared with traditional physical adsorption methods.

For the reasons given above, we selected a biocompatible β-TCP porous scaffold as the base part (TCP) of the composite scaffold, followed by introducing a bioinspired polymerized PDA coating on its surface without complex and harsh chemical reactions. In addition, TCP provides numerous macro/micro pores and a large surface area, which are essential for sufficient PDA coating and local drug delivery purposes. Upon creation of the PDA layer on the scaffold surface, the Wnt signaling activator (BML) is immobilized on the PDA layer by Schiff base formation and the combined effect of physical adsorption, electrostatic interaction, and strong chemical interaction between the PDA and –NH$_2$ of the BML surface. After that, we further utilized carboxymethyl chitosan (CCS) to modify the outermost layer of BML-loaded hybrid films to endow the scaffold with more functional biological cues. CCS is a water-soluble derivative of chitosan; the carboxymethyl group in its molecule is negatively charged, and a positively charged drug can produce electrostatic interactions [22]. Therefore, BML released from the hybrid films could be further restricted in the scaffold for sustained release by electrostatic interactions as well as strong chemical interactions between BML and CCS, which made it useful for long-term stable delivery. Additionally, CCS is an ECM analog with desirable biological properties, such as good biocompatibility, degradability and bioactivity for osteogenesis [23]. To the best of our knowledge, this is the first study on the osteogenesis, angiogenesis, and osteoclastogenesis effects of BML-loaded biofunctionalized TCP scaffolds for robust bone regeneration. Herein, a
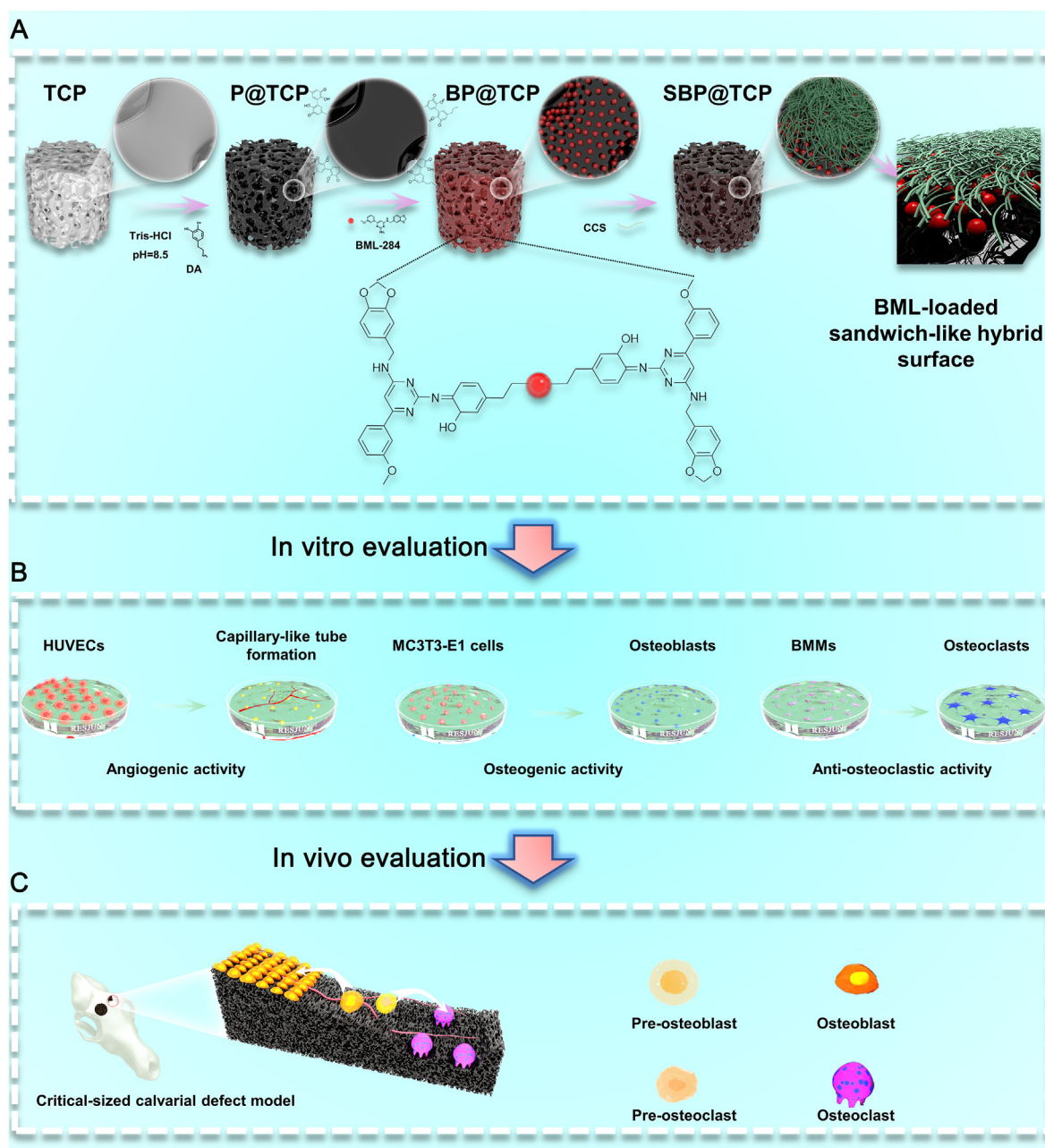
Fig. 1. Schematic illustration of the process used to prepare and evaluate the biofunctionalized TCP-based materials for potential application in bone regeneration. (**A**) Fabrication of a novel surface-modified TCP 3D scaffold with a BML-loaded sandwich-like hybrid surface via bioinspired dopamine chemistry and a self-assembly method. (**B**) In vitro evaluation of the biofunctionalized SBP@TCP scaffolds regulating osteogenesis, angiogenesis, and osteoclastogenesis. (**C**) In vivo evaluation of the biofunctionalized SBP@TCP scaffolds facilitating endogenous bone regeneration through synergistic osteogenic/angiogenic stimulation and osteoclastic inhibition.

BML-loaded sandwich-like surface was prepared as a drug-delivery system to enable the biofunctionalization of BML for pure TCP scaffolds, as shown in Fig. 1. With these merits, we hypothesize that our novel localized delivery platform would integrate multiple biological processes, including osteogenic and angiogenic differentiation promotion, as well as osteoclast differentiation suppression, thereby exerting a synergistic effect on bone healing acceleration. In this study, a bioinspired TCP hybrid scaffold with sandwich-like surface (CCS/BML/PDA) immobilization was prepared, and the physicochemical properties of the scaffold, including three-dimensional (3D) morphology, controlled release of BML, hydrophilicity, protein absorption, mechanical properties, and chemical characterization, were investigated. The cytocompatibility (e.g., cell proliferation, adhesion, migration, infiltration, and spreading),

pro-osteogenic/angiogenic differentiation and anti-osteoclast activity of the scaffold were systematically investigated in vitro. Finally, these scaffolds were evaluated in a rat critical-sized calvarial defect model to determine the in vivo bone repair efficacy and thus suggest potential therapeutic strategies for bone regeneration.

2. Results and discussion

2.1. Preparation and characterization of biofunctionalized scaffolds

An increasing number of physical and chemical methods, such as physical adsorption and covalent binding, have been employed to anchor bioactive molecules onto the bone implant surface to induce osteogenesis
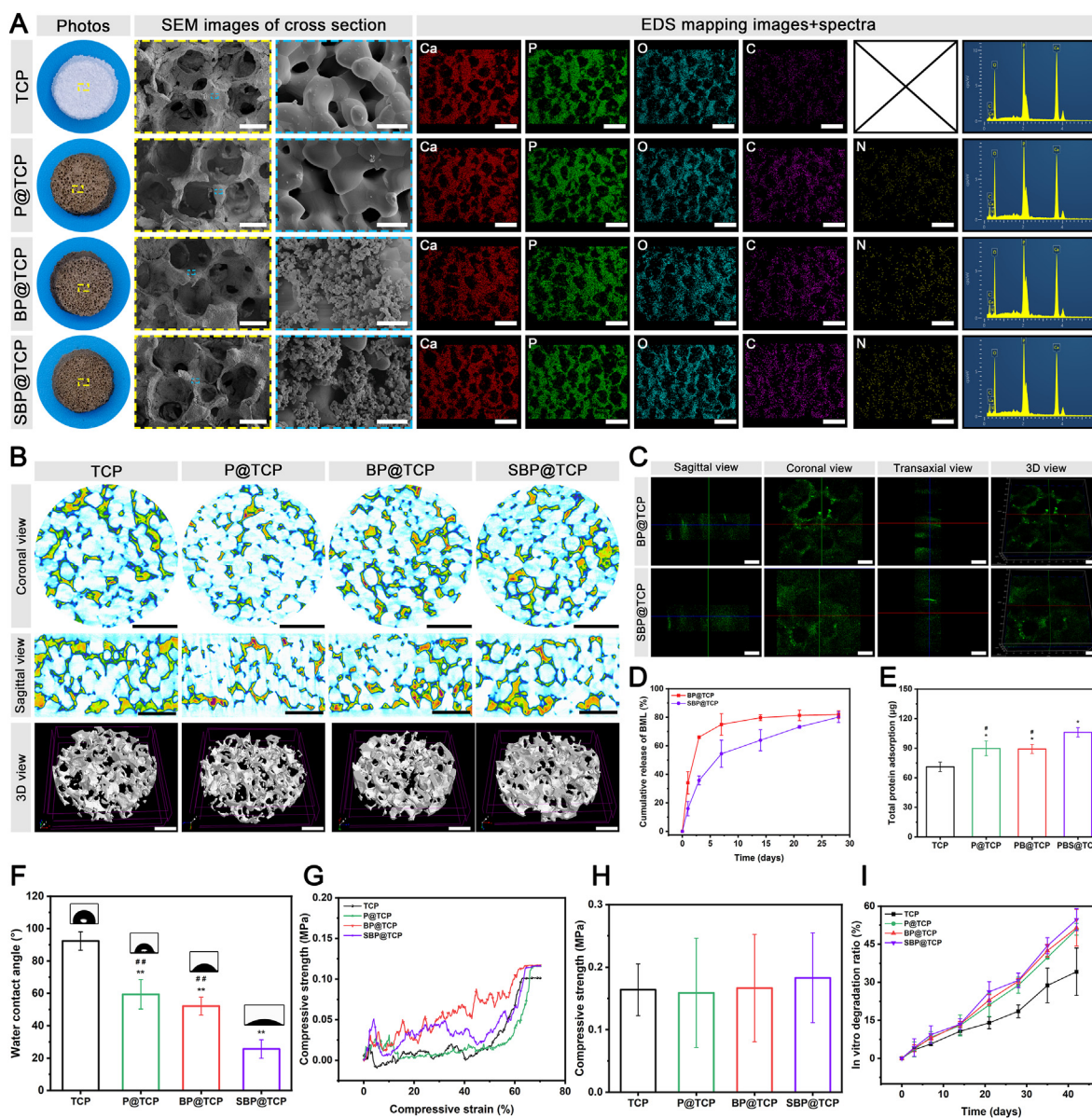
Fig. 2. Characterization of the biofunctionalized scaffolds. (**A**) Representative macroscopic photos, SEM images, EDS elemental mapping and spectra of different TCP-based samples. (**B**) Representative 3D micro-CT images of different TCP-based samples. (**C**) Representative confocal images of BML visualization (green fluorescence) on BP@TCP and SBP@TCP scaffolds. (**D**) The release of BML from BP@TCP and SBP@TCP scaffolds. BML release was monitored for over 4 weeks. (**E**) Protein adsorption on different TCP-based samples. (**F**) Water contact angle changes on different TCP-based samples. (**G**) Representative stress–strain curves of different TCP-based samples under compression. (**H**) Statistical results for the compressive strength at approximately 70% strain. (**I**) In vitro degradation behavior of different TCP-based samples. Scale bar: 200 μm (low-magnification SEM images in A), 5 μm (high-magnification SEM images in A), and 500 μm (EDS mapping images in A), 500 μm (B), and 200 μm (C). Data are presented as the mean ± SD (n = 3). *P < 0.05 and **P < 0.01 indicate significant differences compared with the TCP group. #P < 0.05 and # #P < 0.01 indicate significant differences compared with the SBP@TCP group.

and angiogenesis, thereby promoting bone healing [1,8,24]. However, the difficulty lies in the fact that physical adsorption may not be effective for long-term implantation mainly due to the lower stability of the adsorbed molecules and limited adsorption efficiency, whereas covalent binding often causes a decrease in the bioactive potential of molecules [25]. More importantly, these surface modification methods mainly focus on osteoinduction and the differentiation of osteoblasts while rarely considering the influence of osteoclastogenesis, which also exerts a vital role in bone repair and remodeling. Therefore, the clinical performance of these strategies is poor due to the lack of an ideal drug delivery system and limited bone-forming bioactivities. To this end, we designed and prepared a novel surface-modified TCP 3D scaffold with a BML-loaded sandwich-like hybrid surface via bioinspired dopamine chemistry and a self-assembly method, which possessed synergistic therapy of large bone

defects through the regulation of osteogenesis, angiogenesis, and osteo-clastogenesis. Recently, owing to the versatile adhesion properties, mild synthesis requirements, excellent biocompatibility, and facile immobili-zation of biomolecules, mussel-inspired PDA coatings have been widely used to functionalize material surfaces with various bioactive molecules, including peptides, polymers and proteins [26]. Therefore, according to the intrinsic adhesive properties of polyphenols, a bioinspired polymer-ized PDA coating was formed on a porous TCP surface through oxidative self-polymerization under alkaline conditions. As shown in Fig. 1, the pure TCP scaffold was selected as the base part of the composite scaffold because of its 3D porous structure and favorable biocompatibility, which were conducive to sufficient PDA coating. Based on pure TCP, P@TCP was also prepared by the in situ self-polymerization of dopamine to obtain a PDA biofunctionalized TCP scaffold. Due to the abundant

functional groups (catechol, amine, and imine) of the PDA coating, this biofunctionalized surface has been adopted to interact with many drugs or polymers via multiple interactions, including electrostatic interactions, π-π stacking, hydrogen bonding, and Waals interactions, which have been used for controlled drug release, such as antibiotics, anticancer drugs and even bioactive proteins. Subsequently, the Wnt signaling activator BML was introduced to the surface of the PDA-coated TCP scaffold (BP@TCP) by the interaction between BML ($-NH_2$) and the many functional moieties of PDA (quinone-like structure) as well as the Schiff base reaction between dopamine and BML, which enabled ultra-high BML loading (Fig. S1). Furthermore, due to the presence of amine groups and phenolic hydroxyl groups in the PDA layer, the P@TCP surface can also exhibit a negative charge at high pH and a positive charge at low pH due to protonation (Fig. S2). Accordingly, this would be beneficial for the interaction with the positively charged BML (Fig. S3), together as a sustainable drug release system. To further improve the sustained release behavior and prolong the maintenance time of an effective drug concentration in situ, CCS hydrogel coating was immobilized on the outer layer of the BP@TCP scaffold. The negatively charged carboxymethyl groups of CCS could interact with the BML molecule via electronic interactions and hydrogen bonding, acting as an excellent sustainable drug release device at the injury site. In this context, the immobilization of BML and in situ CCS hydrogel coating proceeded sequentially on the PDA-coated surface via a bioinspired dopamine chemistry and self-assembly approach, ultimately forming a sandwich-like multifunctional surface for large bone defect repair (Fig. 1).

A total four kinds of scaffolds were fabricated for further analysis, including pure β-TCP (TCP) scaffolds, intermediate PDA-coated TCP (P@TCP) scaffolds, BML-loaded P@TCP (BP@TCP) scaffolds and CCS biofunctionalized BP@TCP (SBP@TCP) scaffolds. The appearance, surface topography, and 3D microstructure of these scaffolds prepared in each process were documented with digital photos, scanning electron microscope (SEM), and micro-computed tomography (micro-CT) images. General observation of these scaffolds is shown in Fig. 2A. From the macroscopic photos, we can observe that the introduction of the PDA coating turns the originally white color of the TCP ceramics into light brown and showed no significant change on the surface after modification by the BML and CCS hydrogel coatings. It has been reported that bone-substitute materials should have a proper porous 3D structure with sufficient porosity and pore size to offer enough space for the adhesion, proliferation and differentiation of stem cells, osteocytes, osteoblasts, and vascular endothelial cells [27]. According to the 2D and 3D reconstructed micro-CT images, four kinds of TCP-based scaffolds were displayed to have evenly distributed porous structures on the surface and inside, and there were interconnected structures between the pores (Fig. 2B). Cross-sectional SEM images at various magnifications displayed the morphological features of these 3D scaffolds. As shown in Fig. 2A, all fabricated scaffolds possessed a highly interconnected porous structure constituted by abundant macropores and micropores, highly similar to natural cancellous bone [28]. These structures were not only conducive to new bone ingrowth and rapid blood vessel formation but also provided more adsorption sites for bioactive molecules and improved nutrient and metabolic waste transportation. Moreover, this kind of 3D interconnected porous structure was capable of inducing early osteogenesis from the surrounding cells and tissues through cell adhesion, penetration, proliferation, and tissue ingrowth [29]. SEM images of high magnification also showed that the pure TCP and P@TCP surfaces were homogeneous and smooth, while both BP@TCP and SBP@TCP surfaces were uniformly coated by a thin film of drug particles, suggesting the presence of BML crystals (Fig. 2A). To further demonstrate the elemental composition of the biofunctionalized scaffolds, EDS analysis was performed. As shown in Fig. 2A, the presence of N element was newly detected in the three biofunctionalized scaffolds, and the ratio of N to C was also calculated according to the EDS spectrum. Briefly, the atomic percentages of N and C and the N/C ratio of scaffolds were

increased after modification with PDA. Furthermore, when BML was loaded on scaffolds, both the atomic percentages of N and the N/C ratio further increased. However, after modification with the CCS hydrogel coating, both the atomic percentages of N and the N/C ratio decreased (Table S1). This further confirmed that the modification of PDA, BML and CCS hydrogel coatings proceeded sequentially on the pure TCP scaffold surface. To demonstrate the successful immobilization of the BML molecules, FITC-labeled BMLs were introduced and detected using immunofluorescence methods. As displayed in Fig. 2C, a large amount of uniform fluorescently labeled BMLs adhered to the inside of the scaffold and attached to the inner pore walls, which might further improve cell migration to the inside of scaffolds after implantation. Owing to the open structure and biofunctionalized surface of the scaffold, the BML could penetrate the scaffold's inner surface instead of only forming a coating on the scaffold's outer surface. The density of BML within the BP@TCP and SBP@TCP scaffolds was 18.8 ± 0.5 μg/cm^3 and 18.6 ± 1.2 μg/cm^3, respectively, which provided the first evidence of the high loading efficiency of BML. Sustained release of BML would be beneficial to maintaining an effective drug concentration for local cell behaviors; moreover, it might exert enduring biological effects on the surrounding tissue. The accumulative release profile of BML was measured by HPLC–MS (Fig. S4) according to a standard curve (Fig. S5). As shown in Fig. 2D, the BML-loaded SBP@TCP scaffold maintained sustained release over a period of 28 days. This stable sustained release trend may have resulted from synergistic contributions from the PDA and CCS modification. In comparison, BML release from the BP@TCP scaffold used as a control reached 75% on day 7, possibly due to the fast oxidation of the PDA coating, thus causing the release of surficial BML molecules. These results indicated that the prepared SBP@TCP scaffold had the ability to sustain the long-term and stable release of BML molecules, which play a crucial role in subsequent biological performance.

In addition to effectively delivering BML in a sustained manner, the protein loading capacity of these scaffolds was also investigated. As shown in Fig. 2E, these PDA-biofunctionalized scaffolds had higher protein adsorption capacity (SBP@TCP: 106 ± 4.6 μg; BP@TCP: 89.1 ± 4.5 μg; P@TCP: 89.7 ± 7.4 μg) than the pure TCP samples (71.1 ± 4.8 μg), of which the SBP@TCP scaffolds exhibited the highest adsorption capacity. Simultaneously, there was no obvious difference in protein adsorption between the BP@TCP and P@TCP scaffolds. The binding of proteins to substrate surfaces occurs prior to cell attachment and is dominated by surface physicochemical properties, e.g., surface microstructure, roughness, and wettability. In this work, the significant increase in the protein loading ratio resulted from the superior protein adsorption abilities of PDA and CCS, which exhibited abundant hydrophilic groups such as hydroxyl and carboxyl groups. In bone repair applications, the adsorbed proteins on the scaffold or implant surface are the crucial regulators of many vital signaling pathways, which trigger various intracellular events, leading to cell attachment, spreading, and proliferation [30]. Altogether, our sandwich-like hybrid surface not only allowed for the facile immobilization of bioactive factors to preserve their bioactivity and achieve a long-term, stable and slow-release pattern but also possessed superior protein adsorption capacity, showing great potential as a useful platform for drug delivery.

Then, X-ray diffraction (XRD) analysis was carried out to detect the phase composition of each TCP-based sample. The results indicated that the peaks of the four samples were all similar to typical β-TCP patterns (JCPDS card: No. 09-0169), suggesting that the main component of the samples was β-TCP without an impurity phase (Fig. S6A). Thus, XRD patterns revealed that the three biofunctionalized scaffolds had the same crystal structure as pure β-TCP, which implied that the introduction of PDA, BML, and CCS did not affect the structural integrity or crystallinity of β-TCP. The Fourier transformed infrared (FTIR) spectra of these scaffolds are shown in Fig. S6B. Several absorption peaks representing crystalline phosphate (547, 605, 968, 1018, 1037, and 1122 cm^{-1}) were detected in all four scaffolds, indicating that the majority of them were similar. In particular, the peak at 968 cm^{-1} is a representative indication

of crystalline HA. However, no additional peaks for PDA or CCS were detected in these scaffolds, indicating that the vibration bands of PDA and CCS may overlap with those of β-TCP due to a relatively low content of PDA and CCS in crystals. Notably, the stretching band of PO_4^{3-} at 1037 cm^{-1} in pure TCP shifted to 1031 cm^{-1} in P@TCP, implying the formation of a strong interaction between the CaP phase and PDA constituent. Furthermore, the successful modification of PDA was also verified using Raman spectral analysis (Fig. S7). It is clearly revealed that two broad peaks situated at 1365 and 1559 cm^{-1} were detected, which were assigned to the stretching and deformation of the aromatic ring from PDA, respectively. The surface chemical components of these scaffolds were confirmed by X-ray photoelectron spectroscopy (XPS) analysis, and the results are presented in Fig. S6C. The XPS spectrum of the pure TCP scaffold displayed the characteristic peaks attributed to Ca2s, Ca2p, P2s, P2p, and O1s and the impurity peak attributed to C1s. Except for the abovementioned elements, the N1s peak was newly observed in the intermediate coating of PDA. Likewise, the C1s spectrum of pure TCP can be deconvoluted into C–C, whereas two new curves for C–N/C–O and C=O bonds were detected in P@TCP, indicating that PDA was successfully modified on the TCP scaffold (Figs. S8A–D). Moreover, the XPS spectra also confirmed the loading of BML into the BP@TCP scaffold. With the immobilization of BML, compared with P@TCP, the intensity and half peak width of the peak corresponding to the N1s increased significantly in the survey spectrum of BP@TCP, implying that more nitrogen with different chemical states was present. Moreover, the shift of the N1s peak from 399.5 to 399.3 eV was observed in the BP@TCP scaffold group owing to the presence of amino groups in the BML layer (Fig. S8E). After coating with CCS hydrogel, the N1s peak shifts from 399.3 eV to 399.4 eV, which may be related to the electrostatic interaction and hydrogen bond between BML and CCS. In addition, compared with BP@TCP, the increased intensity and more complex shape of the C1s peak were observed in the SBP@TCP group, confirming that the CCS hydrogel coating introduced into SBP@TCP contained more carbons of different chemical states. These data further validated the successful construction of our sandwich-like drug delivery system. Then, we performed thermal gravimetric analysis (TGA) to quantify the amount of organic phase loaded onto the pure TCP scaffold by comparing the differences in the total weight loss among TCP, P@TCP, BP@TCP, and SBP@TCP. The results revealed that 1.42 wt% PDA, 0.12 wt% BML, and 1.07 wt% CCS were immobilized on the P@TCP, BP@TCP, and SBP@TCP scaffolds, respectively (Fig. S6D). This further indicated efficient PDA-mediated immobilization of BML and CCS on the surface of SBP@TCP.

Moreover, the basic structural properties of these scaffolds were also investigated. As shown in Fig. S9, all TCP-based scaffolds had similar average pore sizes (~350 μm) and total porosities (~68%), which are within the range of cancellous bone (50%–95%) [31,32]. There was no significant difference among them, which demonstrated that neither the addition of PDA nor the immobilization of BML and CCS had obvious effects on the scaffold's pore size and porosity. These 3D stereoscopic structures and high porosity are prerequisites for nutrition transport and exchange during cell ingrowth and bone tissue reconstruction [13]. Furthermore, numerous studies have indicated that engineered 3D scaffolds with pore sizes ranging from 100 μm to 500 μm and porosities greater than 50% are preferred as bone repair scaffolds because they have a desirable angiogenic capacity and can result in direct osteogenesis, thus accelerating the bone repair process [31]. On the basis of these results, our newly developed biofunctionalized scaffolds had excellent porosity, pore size, and an interconnected porous structure, which is helpful for achieving rapid angiogenesis and osteogenesis.

The hydrophilicity of the different samples was determined by water contact angle measurements. As shown in Fig. 2F, the water contact angles of pure TCP and P@TCP were 92.3 ± 5.7° and 59.5 ± 9.1°, respectively. Apparently, the introduction of PDA improved the scaffold hydrophilicity because PDA was rich in hydrophilic functional groups, such as amino-functional and carboxyl-functional groups, which was

similar to results from previous studies [33]. The water contact angle of the BP@TCP sample surface was 52.2 ± 5.6°, indicating the negligible influence of BML on the hydrophilicity of the biofunctionalized coating. After CCS functionalization, the average water contact angle of SBP@TCP was reduced up to 25.6 ± 5.7°, which would be beneficial for cell adhesion and infiltration of body fluids. The abundant amino, carboxyl, and hydroxyl groups on the SBP@TCP surface were envisioned to enhance the hydrophilicity of the substrate, resulting in a lower water contact angle. Previous studies demonstrated that hydrophilic scaffolds have a better capacity for initial cell adhesion in vitro and effectively penetrate the host cell in vivo, eliciting the success of bone-implant integration [34]. Accordingly, the SBP@TCP scaffold manifested superior hydrophilicity, which facilitated the absorption of bioactive molecules and proteins after biomaterial implantation in vivo, thus improving the subsequent cell response and cell/substrate interactions.

Compressive tests were conducted to assess the mechanical behavior of the pure TCP, P@TCP, BP@TCP, and SBP@TCP scaffolds. For successful bone regeneration, biomaterials implanted in bone defects should provide basic structural support and space for facilitating cell infiltration and tissue ingrowth [35]. To verify the mechanical properties of the fabricated scaffolds, compressive tests were performed. Fig. 2G shows the representative compression stress–strain curves and the mechanical properties of all scaffolds. The results indicated that all four TCP-based scaffolds possessed similar compressive strengths (Fig. 2H) and elastic moduli (Fig. S10), showing no significant difference. Altogether, we found that the introduction of PDA, BML, and CCS hydrogel coating had no appreciable impact on the overall mechanical properties of all TCP-based scaffolds, which may be due to the low mechanical support provided by these components. Additionally, the compressive strength of all scaffolds was greater than 0.1 MPa, which was beneficial for facilitating cellular proliferation and osteogenic differentiation, as demonstrated in previous reports [36]. Importantly, earlier research demonstrated that the compressive strength of human cancellous bone ranges from 0.22 to 10.44 MPa [23]. Thus, the biofunctionalized scaffolds could be suitable for non-load bearing bone regeneration applications, such as regeneration skull cranial bones.

The appropriate biodegradability of tissue engineering scaffolds is another pivotal prerequisite for bone regeneration applications. Typically, biomaterials should gradually degrade after providing mechanical support for cell infiltration and tissue ingrowth and should not hinder tissue regeneration during the process of bone repair [37]. Fig. 2I shows the in vitro biodegradation profile of these scaffolds calculated using the weight loss method. During the whole incubation period, all scaffold samples exhibited a relatively sustained weight loss. In the first 14 days, all four scaffolds showed no apparent weight loss (~15%). With increasing incubation time, the weight of the three biofunctionalized scaffolds began to decline at an accelerated rate, of which SBP@TCP exhibited a faster degradation rate than those of the other scaffolds. This might have resulted from the superior hydrophilic surface modified by PDA and CCS, which was consistent with the literature [33]. Additionally, active oxygen, such as oxygen species and free radicals, triggers the oxidative biodegradation of PDA, thus accelerating the material hydrolytic degradation, making it suitable for long-term implantation.

2.2. In vitro cytocompatibility evaluation of biofunctionalized scaffolds

Previous studies have validated that a proper concentration of BML can promote cell proliferation and differentiation [38]. The optimal BML loading concentration was determined via in vitro osteogenic differentiation of MC3T3-E1 cells and cytotoxicity assays. As shown in Fig. S11, when the concentration was set at 50 μg/mL, BML exhibited the greatest osteogenic induction of MC3T3-E1 cells, while showing no significant cytotoxicity. On the basis of these results, BML at a concentration of 50 μg/mL was chosen for the construction of BML-loaded biofunctionalized scaffolds.

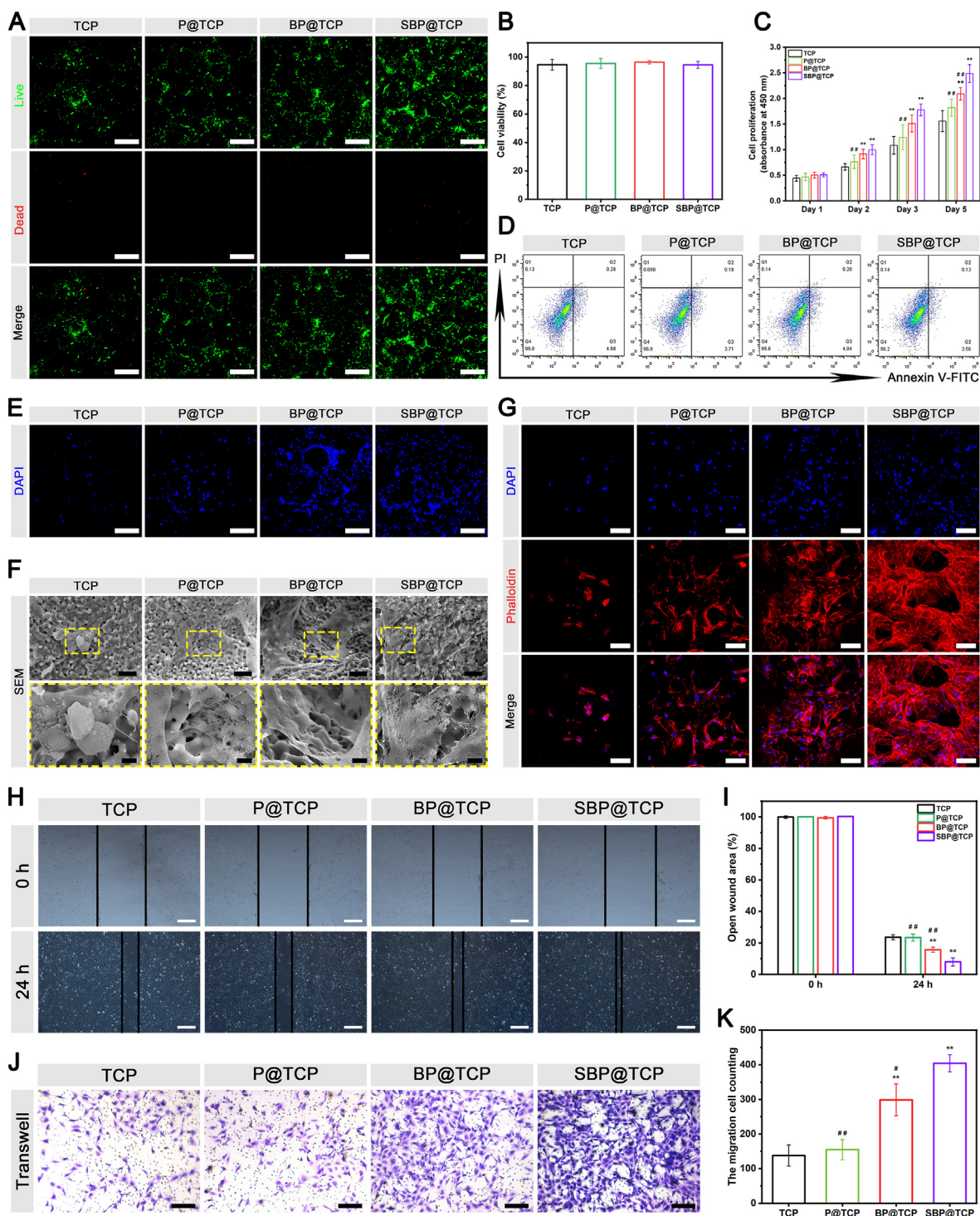To achieve effective bone repair, bioactive scaffolds used for bone

Fig. 3. In vitro cytocompatibility of the biofunctionalized scaffolds. (**A-B**) Representative confocal images of live/dead staining and statistical analysis of MC3T3-E1 cells. (**C**) Cell proliferation in MC3T3-E1 cells for 1, 2, 3, and 5 days. (**D**) Cell apoptosis in MC3T3-E1 cells after 3 days. (**E**) Cell adhesion in MC3T3-E1 cells after 6 h. (**F**) Representative SEM images of MC3T3-E1 cells incubated for 3 days on different samples. (**G**) Representative confocal images of F-actin cytoskeleton staining for MC3T3-E1 cells incubated for 7 days on different samples. (**H–I**) Representative wound healing migration images and quantitative analysis of the migratory ability of MC3T3-E1 cells in the scratch assay. (**J-K**) Representative Transwell migration images and quantitative analysis of the migratory ability of MC3T3-E1 cells in the Transwell assay. Scale bar: 250 μm (A, E), 20 μm (low-magnification SEM images in F), 5 μm (high-magnification SEM images in F), 100 μm (G), 500 μm (H), and 200 μm (J). Data are presented as the mean ± SD (n = 3). *$P < 0.05$ and **$P < 0.01$ indicate significant differences compared with the TCP group. #$P < 0.05$ and # #$P < 0.01$ indicate significant differences compared with the SBP@TCP group.

regeneration should be nontoxic or slightly toxic and exhibit good cytocompatibility, which is a fundamental prerequisite in bone regeneration applications [39]. In this study, MC3T3-E1 cells were selected as the model cells due to their stable performance and good experimental

reproducibility and are widely used in cytotoxicity evaluation, osteoblastic differentiation, osteoblastic mechanisms, and mineralization in vitro [6,40]. To evaluate the cytocompatibility of these scaffolds in vitro, live/dead staining of MC3T3-E1 cells seeded on these scaffolds was
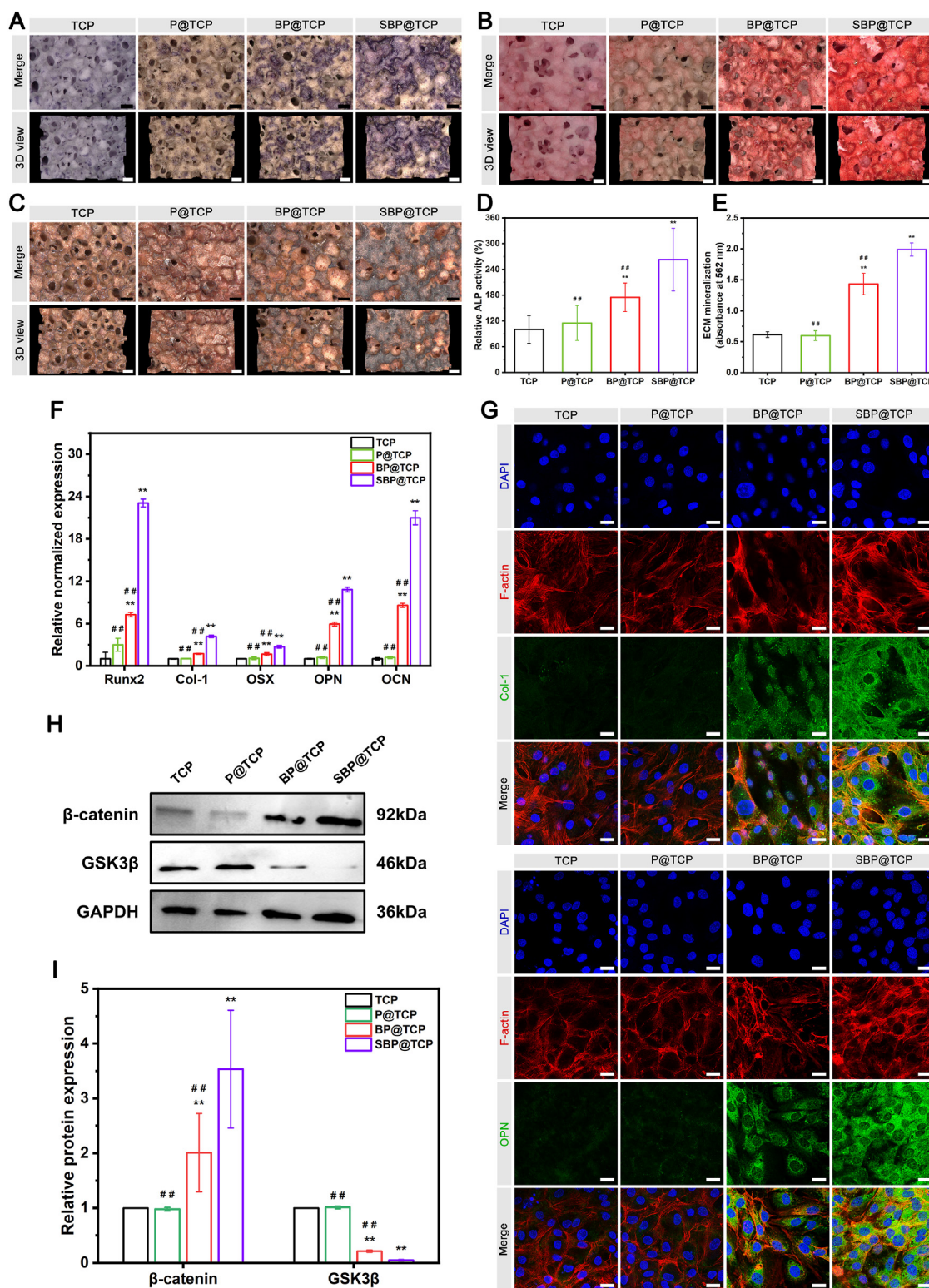
Fig. 4. In vitro osteogenic activity of the biofunctionalized scaffolds. (**A-C**) Representative images of ALP staining, ARS staining, and von Kossa staining on different scaffold samples after 7, 14, and 21 days of cell seeding, respectively. (**D-E**) Quantitative evaluation of ALP activity and matrix mineralization of MC3T3-E1 cells on different scaffold samples. (**F**) Relative mRNA expression levels of osteogenesis-related markers, including Runx2, Col-1, OSX, OPN, and OCN, after culturing for 7 days. (**G**) Representative immunofluorescent staining images of osteogenic Col-1 and OPN proteins after culturing for 7 days. Target protein, F-actin, and cell nuclei were labeled with fluorescent green, red, and blue, respectively. (**H**) Representative western blot results for β-catenin and GSK3β from MC3T3-E1 cells co-cultured with various scaffolds. (**I**) Quantitative analysis of corresponding protein levels acquired from western blot. Scale bar: 250 μm (A, B, C), 25 μm (G). Data are presented as the mean ± SD (n = 3). *P < 0.05 and **P < 0.01 indicate significant differences compared with the TCP group. #P < 0.05 and ##P < 0.01 indicate significant differences compared with the SBP@TCP group.

performed after 3 days of co-culture. As shown in Fig. 3A and B, the live/dead staining results demonstrated that large quantities of living cells were enriched within the pore walls on the scaffolds (cell viability >95%), which indicated that all scaffolds had excellent cytocompatibility. In addition, the cell number was positively correlated with the fluorescence intensity, further confirming that there were a large number of living cells showing green color in the SBP@TCP group on day 3. This finding was primarily attributed to the porous TCP-based scaffolds providing sufficient cell-growth space. Moreover, according to the CCK-8 assay results (Fig. 3C), MC3T3-E1 cells continuously proliferated on all scaffolds, and insignificant differences were observed between scaffolds at 1 day. Cells exhibited better proliferation on BP@TCP and SBP@TCP than TCP and P@TCP on days 2, 3, and 5. After co-culture for 5 days, the optical density (OD) values of P@TCP, BP@TCP, and SBP@TCP were 1.17, 1.34, and 1.59 times higher than that of TCP, respectively. The enhanced cell proliferation was likely due to BML release into the cell medium. As an efficient WNT agonist, BML can effectively promote the activation of the Wnt/β-catenin signaling pathway and stimulate the expression of growth factors, such as BMP and VEGF, in osteoblasts. Previous studies have shown that these factors can promote the proliferation and recruitment of osteoblasts [41]. To further confirm the CCK-8 and live/dead staining results, flow cytometry was performed. As shown in Fig. 3D, the results revealed that MC3T3-E1 cells maintained a high percentage of viable cells and a negligible apoptosis rate on all four scaffolds. These results confirmed that biofunctionalized SBP@TCP scaffolds not only had good cytocompatibility but could also further promote cell proliferation, which provides a basis for promoting bone repair.

It has been reported that cellular adhesion capability is key to the biological responses of cells to implanted biomaterials and is beneficial for the subsequent cell behavior, morphogenesis, and ultimate tissue response [13]. Therefore, we first investigated the initial cell adhesion of MC3T3-E1 cells via DAPI staining. As shown in Fig. 3E, the three biofunctionalized scaffolds showed higher cell adhesion ability than pure TCP after 6 h of co-culture. Notably, the number of adhesive cells in SBP@TCP was significantly higher than that in other groups, followed by P@TCP, BP@TCP, and pure TCP scaffolds (Fig. S12). There was no significant difference between the P@TCP and BP@TCP groups. Benefiting from the presence of cell adhesive PDA, biocompatible CCS hydrogel coating, and biomimetic 3D porous structure, the SBP@TCP scaffolds could greatly facilitate cell attachment, survival, and growth. As the main components of the biofunctionalized surface, PDA and CCS were demonstrated to facilitate the initial cell adhesion of MC3T3-E1 cells, yet the limited release of BML from the biofunctionalized surface did not have an adverse impact on the initial cell adhesion.

To effectively assess the cell attachment and spreading morphology on these scaffolds, SEM observation was performed, and the results are displayed in Fig. 3F. The SEM images revealed that all scaffolds were capable of supporting cell adhesion, proliferation and growth owing to the interconnected 3D porous architecture that offered a favorable microenvironment. It is worth noting that cells cultured on the three biofunctionalized scaffolds exhibited a well-spread morphology with numerous filopodia extensions, whereas cells on the TCP scaffold rapidly stretched and showed an oval shape (Fig. S13). Moreover, the SEM images also revealed that the cells cultured on the SBP@TCP scaffold tended to have more pseudopodia and developed a more spindle-like and elongated morphology, indicating the formation of strong interactions with the surface microstructures. The interaction between MC3T3-E1 cells and these scaffolds confirmed that the modified 3D scaffolds not only had no cytotoxicity but also promoted the 3D growth of cells. This is mainly due to the superior surface hydrophilicity, high porosity, well interconnected pore network structure, and biofunctionalized surface properties.

Subsequently, we evaluated cell extension by CLSM after staining for F-actin in the cytoskeleton, as shown in Fig. 3G. Corresponding to the SEM results, the actin filaments of MC3T3-E1 cells co-cultured with

biofunctionalized scaffolds possessed abundant branched stretching directions with long filopodia, while the cells on pure TCP showed polygonal, short and fat shapes with much fewer filopodia. Among them, the SBP@TCP scaffold could significantly support cell growth and further stimulate cell ingrowth into scaffolds via well-interconnected macropores and favorable surface properties, indicating increased proliferation status. Additionally, MC3T3-E1 cells presented good adhesion and extension of cells along the surface of the SBP@TCP scaffold surface, which were tightly linked with each other to form integrated complexes. These well-developed cell cytoskeletons and clusters further undergo osteogenic differentiation and tissue mineralization to promote bone formation. Thus, compared with pure TCP, P@TCP, and BP@TCP, the SBP@TCP scaffold not only further promoted cell attachment but also better promoted cell growth and spreading, which was essential for osteogenesis.

Furthermore, the effect of these scaffolds on MC3T3-E1 cell migration was investigated. After co-culture with these scaffolds for 7 days, a wound healing assay and Transwell assay were applied to analyze the migration and infiltration of MC3T3-E1 cells. Fig. S14 is a schematic of the co-culture Transwell system used to investigate the migration abilities of MC3T3-E1 cells. The wound scratch assay showed that the MC3T3-E1 cells migrated significantly faster in the BML-immobilized scaffold group than in all other groups (Fig. 3H). Interestingly, for the SBP@TCP group, the positive impact on cell migration was stronger than that for the BP@TCP group. In contrast, there was no obvious difference in cell migration between the TCP and P@TCP groups (Fig. 3I). Simultaneously, the Transwell assay revealed that the number of MC3T3-E1 cells that infiltrated the BML-immobilized scaffold groups was much higher than that in the other groups (Fig. 3J). The number of cells that migrated from the SBP@TCP group was significantly higher than that from the BP@TCP group (Fig. 3K). The combination of BML and CCS hydrogel coating exhibited stronger chemotactic ability than the single BML immobilization, which could be ascribed to the synergistic effect of PDA and CCS hydrogel coating regulation sustained release of BML. Therefore, BML released from the biofunctionalized scaffolds could stimulate MC3T3-E1 cell migration and infiltration, and the BML-loaded sandwich-like surface further enhanced cell migration. Taken together, the above results demonstrated that SBP@TCP could provide a highly biocompatible microenvironment for MC3T3-E1 cell adhesion, proliferation, migration, spreading, and growth through their biofunctionalized surface properties, thus exhibiting great potential for orthopedic implants.

2.3. In vitro evaluation of osteogenesis

The osteogenesis of cell-loaded constructs is critical for bone regeneration applications. Ideal bone implants should also display favorable osteogenic activity beyond their good cytocompatibility [42]. Encouraged by the above results, we assessed the impact of these biofunctionalized scaffolds on osteogenic differentiation in vitro. In this study, ALP activity, calcium deposition, and the expression of osteogenic-related genes and proteins were examined to investigate the osteogenesis ability of MC3T3-E1 cells on the sample surfaces.

Previous reports demonstrated that ALP is an early osteogenic marker of cell maturation and calcification, and the high ALP activity indicates obvious bone ECM synthesis and a prominent osteogenic differentiation effect toward osteoblasts [4]. As depicted in Fig. 4A, the ALP activity on the BP@TCP and SBP@TCP scaffolds was evidently higher than that of the pure TCP and P@TCP scaffolds after 7 days of co-culture, indicating that the immobilization of BML was more conducive to inducing osteogenic differentiation of the MC3T3-E1 cells. In particular, MC3T3-E1 cells in the SBP@TCP scaffold showed the highest ALP activity, followed by the BP@TCP scaffold, and this was in accordance with our previous conclusions and hypothesis (Fig. 4D). Although the ALP activity in the P@TCP group was slightly increased compared with that in the pure TCP group, the difference was not significant. These results further indicated that the SBP@TCP scaffold with sustained release of BML
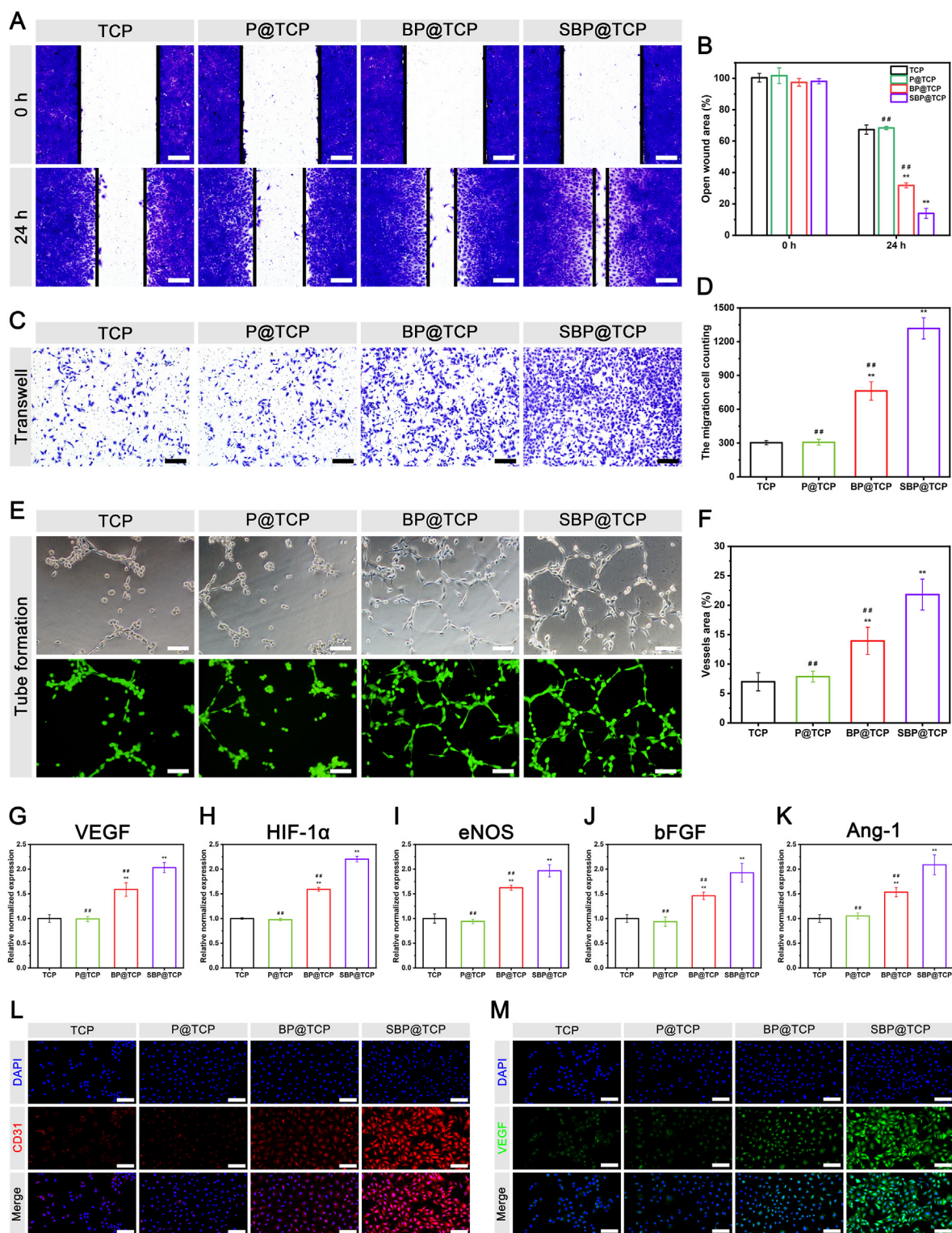
Fig. 5. In vitro angiogenic activity of the biofunctionalized scaffolds. (**A-B**) Representative wound healing migration images and quantitative analysis of the migratory ability of HUVECs in the scratch assay. (**C-D**) Representative Transwell migration images and quantitative analysis of the migratory ability of HUVECs in the Transwell assay. (**E**) Representative optical and fluorescence images of HUVEC tube formation after culturing for 8 h. (**F**) Quantitative analysis of the vessel percentage area of vascular tube formation. (**G-K**) Relative mRNA expression levels of angiogenesis-related markers, including VEGF, HIF-1α, eNOS, bFGF, and Ang-1, after culturing for 7 days. (**L-M**) Representative immunofluorescent staining images of angiogenic CD31 (red) and VEGF (green) proteins after culturing for 7 days. Cell nuclei were labeled with fluorescent blue. Scale bar: 200 μm (A), 100 μm (E), and 100 μm (L, M). Data are presented as the mean ± SD (n = 3). *P < 0.05 and **P < 0.01 indicate significant differences compared with the TCP group. #P < 0.05 and ##P < 0.01 indicate significant differences compared with the SBP@TCP group.

molecules and CCS coating was more effective in inducing MC3T3-E1 cell differentiation toward an osteogenic trend.

It is well acknowledged that in the differentiation process of osteoblasts, collagen secretion is helpful for the formation of the bone extracellular matrix and in connections between cell surface receptors and ECM proteins [3]. Being recognized as an important morphological manifestation of osteogenic function, Sirius Red staining was also performed to verify the osteogenesis capabilities of MC3T3-E1 cells in vitro. Similarly, after 14 days of co-culture, Sirius Red staining results demonstrated that collagen secretion was significantly improved when the MC3T3-E1 cells were cultured on the BML-immobilized scaffolds compared with that on the P@TCP and BP@TCP scaffolds (Fig. S15). Notably, abundant collagen secretion was detected in the SBP@TCP scaffold, which was made by a combinational effect of BML and CCS. Studies have demonstrated that sufficient amounts of collagen synthesis are capable of significantly promoting tissue remodeling in the early stages of osteogenesis, thereby promoting bone regeneration [43]. These results clearly validated that the SBP@TCP scaffold remarkably promoted collagen secretion, which was beneficial for bone healing.

Calcium deposition, namely, biomineralization, is an important marker to evaluate the later stage of osteogenesis. To directly observe calcium deposition, the MC3T3-E1 cell-loaded constructs were subjected to ARS and von Kossa staining after co-culture for 14 and 21 days, respectively. In line with the ALP activity results, the BP@TCP scaffold showed a significantly higher level of calcium deposition that was homogeneously distributed on the scaffold surface and expressed more mineralized matrix than the TCP and P@TCP scaffolds, indicating that BP@TCP possesses osteogenic advantages (Fig. 4B and C). For the SBP@TCP scaffold, which contained both BML and CCS, synergistic effects were exhibited to enhance osteogenesis to a significantly highest level among all scaffold groups. The quantitative results were consistent with the staining results (Fig. 4E). Overall, the results demonstrate that the BML-immobilized biofunctionalized TCP surface had a superior osteoinductive capacity, and the introduction of the CCS hydrogel coating further enhanced the osteogenic differentiation ability of MC3T3-E1 cells.

To further validate these results, we employed a qRT–PCR assay to examine the expression of osteogenesis-related genes after co-culturing with different scaffolds for 7 days. As illustrated in Fig. 4F, the in vitro experimental results suggested that both BML-loaded scaffolds could upregulate the expression of osteogenesis-related genes in MC3T3-E1 cells, which may be beneficial for accelerating bone defect repair. It is universally acknowledged that the physiological process of osteogenesis includes a large number of regulators, such as Runx2, Col-1, OPN, OCN, and OSX. Runx2 is a member of the runt homology domain family of transcription factors, which plays a key role in the regulation of osteoblast gene expression, and Runx2 can upregulate the expression of Col-1 and OCN [44]. OSX, also known as Sp7, is a zinc finger-containing osteoblast-specific transcription factor. It is specifically expressed in all developing bones and is essential for bone formation [17]. OPN and OCN are important late-stage osteogenic markers. OPN is a kind of glycosylated protein that is involved in the bone remodeling process as well as in biomineralization; OCN, secreted by osteoblasts, plays a specific role in MSC differentiation and mineralization [42,45]. Previous studies have also demonstrated that BML can effectively activate the Wnt/β-catenin signaling pathway, an important pathway involved in osteogenic differentiation [46]. Remarkably, the expression of OPN and OCN was dramatically higher in MC3T3-E1 cells on the SBP@TCP scaffold than on the BP@TCP scaffold, implying that sustained release of BML and CCS modification synergistically enhanced the osteogenic effect eventually. These results demonstrated that the SBP@TCP scaffold is a promising platform for osteogenic differentiation.

Immunofluorescence staining of Col-1 and OPN was conducted to confirm osteogenic protein expression in MC3T3-E1 cells. As depicted in Fig. 4G, Col-1 protein (green) was observed to be abundant in the BP@TCP and SBP@TCP groups. In comparison, a lower content of Col-1

proteins was observed in both the pure TCP and P@TCP groups, with no significant difference. Further immunofluorescence staining of OPN showed a similar trend, of which the highest protein contents were observed in the SBP@TCP group, followed by the SBP@TCP group. Few OPN proteins were also observed in the pure TCP and P@TCP groups at similar levels. Col-1 is the main component of organic matrices in bone tissue, and it is closely related to bone remodeling [33]. OPN, a secreted phosphoprotein, plays a fundamental role in bone metabolism and homeostasis [47]. Both qRT–PCR and immunofluorescence staining results showed that SBP@TCP significantly induced the expression of osteogenic factors that are crucial in the process of osteogenesis. Quantitative analysis of fluorescence intensity showed a significantly higher amount of Col-1 and OPN content for the SBP@TCP group, as presented in Fig. S16. The SBP@TCP scaffold with a 3D biomimetic porous structure not only provides a favorable microenvironment for cell behavior but also delivers bioactive BML in a sustained release manner. In addition, as a component of the SBP@TCP scaffold, CCS has been demonstrated to enhance the osteogenic differentiation of MC3T3-E1 cells. Functional groups introduce negative charges to the CCS surface, creating an electrically charged microenvironment suitable for bone defect repair, as demonstrated in previous reports [22]. These factors contribute to the characteristics of the SBP@TCP scaffold, such as its promotion of adhesion and proliferation of MC3T3-E1 cells and acceleration of their osteogenic differentiation in vitro.

The Wnt/β-catenin signaling pathway plays a vital role in regulating cell metabolism and differentiation during bone regeneration [17]. Given the Wnt/β-catenin signaling activation by BML released from BML-biofunctionalized scaffolds, the protein levels of several key markers in Wnt/β-catenin signaling, including β-catenin and GSK3β, were also determined using Western blot analysis. As shown in Fig. 4H and I, the protein expression levels of β-catenin in both the BP@TCP and SBP@TCP groups were significantly higher than those in the pure TCP and P@TCP groups. Through comparison among BML-biofunctionalized groups, there was a most significant enhancement for SBP@TCP scaffold group in β-catenin expression. Moreover, compared with the pure TCP and P@TCP scaffolds, the levels of GSK3β, which negatively regulates the β-catenin signal, were significantly decreased in the BML-biofunctionalized groups, especially SBP@TCP. These results further suggested that the biofunctionalized SBP@TCP scaffold can effectively release BML to activate the Wnt/β-catenin pathway, thereby promoting cell growth and osteogenic differentiation.

2.4. In vitro evaluation of angiogenesis

Angiogenesis is tightly coupled with osteogenesis during the process of bone growth, development, remodeling and repair. In these processes, the formation of a vascular network is vital for achieving functional bone regeneration because it is essential for cell recruitment, cytokine secretion and the transportation of oxygen, nutrients and metabolic waste [8]. ECs participate in the whole process of vascularization, and changes in their migration and function affect angiogenic activity; thus, in this study, HUVECs were used to investigate in vitro angiogenesis. As mentioned previously, the activation of the Wnt/β-catenin signaling pathway was revealed to enhance not only osteogenesis but also angiogenesis by promoting EC migration, differentiation, and tubule-like formation [48]. Similar to the results of MC3T3-E1 cells, all of the as-prepared TCP scaffolds could effectively support HUVEC adhesion, proliferation, and F-actin assembly (Fig. S17), which provided a preliminary basis for the verification of angiogenic performance. Commonly, the first step of vascularization is the recruitment of ECs to facilitate the formation of new blood vessels. To assess the chemotactic response of the HUVECs to these scaffolds, scratch wound healing and Transwell migration assays were performed. As depicted in Fig. 5A–D, the sustained release of BML from both BP@TCP and SBP@TCP scaffolds has a positive effect on HUVEC migration and infiltration, which is conducive to angiogenesis in the process of bone healing and repair. In
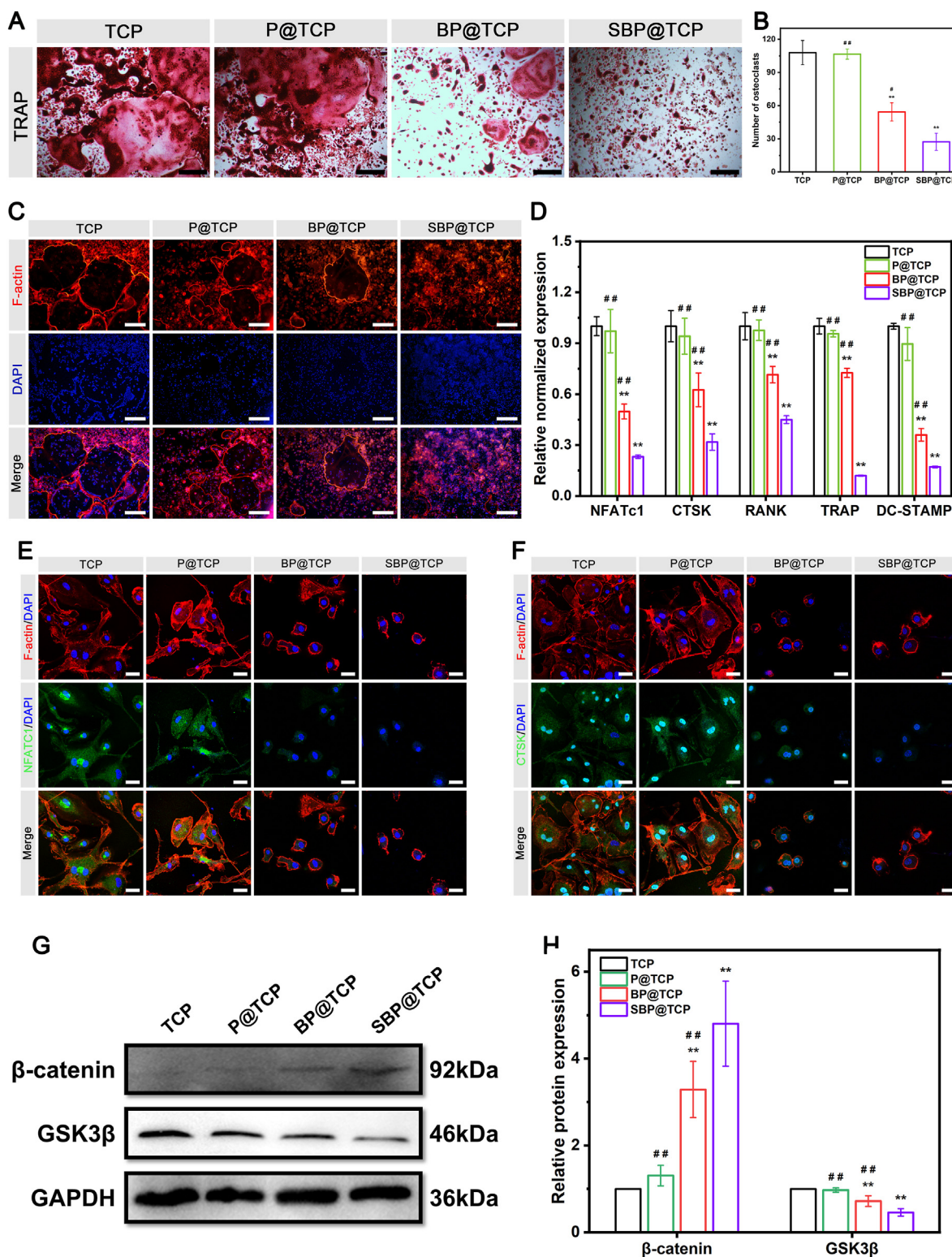
Fig. 6. In vitro anti-osteoclastic activity of the biofunctionalized scaffolds. (**A-B**) Representative TRAP staining images and quantitative analysis results. (**C**) Representative images of the F-Actin ring formation assay. (**D**) Relative mRNA expression levels of osteoclastogenesis-related markers, including NFATc1, CTSK, RANK, TRAP, and DC-STAMP, after culturing for 3 days. (**E-F**) Representative immunofluorescent staining images of osteoclastic NFATc1 and CTSK proteins after culturing for 3 days. Target protein, F-actin, and cell nuclei were labeled with fluorescent green, red, and blue, respectively. (**G**) Representative western blot results for β-catenin and GSK3β from BMMs co-cultured with various scaffolds. (**H**) Quantitative analysis of corresponding protein levels acquired from western blot. Scale bar: 50 μm (A), 100 μm (C), and 25 μm (E, F). Data are presented as the mean ± SD (n = 3). *P < 0.05 and **P < 0.01 indicate significant differences compared with the TCP group. #P < 0.05 and ##P < 0.01 indicate significant differences compared with the SBP@TCP group.

particular, the SBP@TCP scaffold exhibited better performance in enhancing HUVEC migration and infiltration, showing a substantial potential function of promoting angiogenesis. The cell migration capacity in the pure TCP and P@TCP scaffold groups was lower than that of the other groups because there was no effective factor to promote cell migration in the culture medium. These data revealed that the BML released from BML-immobilized TCP scaffolds can stimulate HUVEC migration and infiltration and might provide further evidence for the promotion of vascularization.

The ability of biomaterials to induce vascular formation plays a key role in the reconstruction of defect tissues, as it could provide blood supply that delivers nutrients and oxygen to the impaired tissue, easing uncontrolled inflammation [49]. In this work, a Matrigel tube formation assay was applied to evaluate the vessel-forming capability of HUVECs. As shown in Fig. 5E, HUVECs co-cultured with the BML-immobilized scaffolds had significantly more vascular tube formation, while only a few fragile or incomplete tube-like structures were formed in the pure TCP and P@TCP scaffolds. The percentage of vessel area was significantly increased in the SBP@TCP group compared with all other groups, which confirmed that SBP@TCP treatment could enhance the in vitro angiogenesis of HUVECs (Fig. 5F). The collective findings indicated that BML from both biofunctionalized scaffolds promoted HUVEC migration and rapid formation of blood vessels in vitro. The combination of BML and CCS improved this promotion effect.

Subsequently, the expression of angiogenic-related genes (VEGF, HIF-1α, eNOS, bFGF, and Ang-1) in HUVECs co-cultured with these scaffolds was examined. These genes are key transcription factors for angiogenesis. Compared with the pure TCP and P@TCP scaffolds, BML-immobilized scaffolds significantly improved the expression of angiogenesis-related genes in HUVECs after 7 days of co-culture, suggesting their good in vitro angiogenesis bioactivity (Fig. 5G–K). It was also found that the higher mRNA expression of angiogenesis-related genes was detected in the SBP@TCP group, followed by the BP@TCP group, while there was no significant difference between pure TCP and P@TCP scaffolds. To further verify the ability of BML-immobilized scaffolds to promote angiogenesis, immunofluorescence staining of CD31 and VEGF was performed after 7 days of co-culture. As displayed in Fig. 5L and M, CD31 and VEGF secretion from HUVECs in the BP@TCP and SBP@TCP groups was higher than that in the other two groups, which was consistent with the qRT–PCR assay. CD31, also known as platelet endothelial cell adhesion molecule-1, is commonly used to prove the presence of vascular endothelial cells and can be used to evaluate angiogenesis. Moreover, the angiogenesis effect of the SBP@TCP group was better than that of the BP@TCP group, indicating that BML and CCS modification had a synergistic effect on angiogenesis. Notably, the enhanced expression of VEGF was revealed to be coupled with the activation of the Wnt/β-catenin signaling pathway, which subsequently promoted the tube formation of HUVECs in vitro [48]. Overall, these data clearly indicated that BML-loaded TCP scaffolds featured robust angiogenic activity, leading to the enhancement of HUVEC migration and infiltration as well as capillary-like tube formation in vitro, which played a promoting role in the process angiogenesis and osteogenic differentiation of bone repair.

2.5. In vitro evaluation of osteoclastogenesis

It is well known that, except for osteoblasts, osteoclasts also play indispensable roles during bone healing, while an adequate reduction in osteoclastogenesis may be preferable for bone regeneration [50]. Therefore, evaluating the bone regeneration ability of biomaterials involves not only their osteogenic capacity but also their effects on osteoclast differentiation. Typically, osteoclasts are multinucleated giant cells formed by the fusion of hematopoietic cells of the monocyte-macrophage lineage [51]. In this study, mouse bone marrow macrophages (BMMs) were selected as model cells to assess the effect of these scaffolds on osteoclast activity, as they are the major and important cell source for osteoclast differentiation [4]. According to the results of flow cytometry,

the isolated BMMs presented high percentages of CD11b (approximately 98.1%), confirming the characteristic surface markers of macrophages (Fig. S18). To detect osteoclast differentiation, we first performed TRAP staining, as displayed in Fig. 6A. Obviously, the SBP@TCP groups showed marked suppression of osteoclast formation among all samples, as shown by the significantly decreased area of TRAP-positive cells, followed by the BP@TCP, BP@TCP, and pure TCP groups (Fig. 6B). Next, the formation of the F-actin ring, as the dynamic and characteristic cytoskeletal structures of active osteoclasts, was visualized by F-actin ring immunofluorescence. As shown in Fig. 6C, multinucleated cells with well-defined F-actin rings were observed in the pure TCP and P@TCP groups, whereas the F-actin rings were limited and localized in both the BP@TCP and SBP@TCP groups, which might be primarily attributed to the sustained release of BML from the biofunctionalized scaffolds. It should be noted that the SBP@TCP group showed an excellent inhibitory effect on osteoclast differentiation, as shown by the significantly decreased area of F-actin ring formation (Fig. S19). This was corroborated by the results of the comparison of the other experimental groups, implying that BML may be the most important reason that the hybrid scaffolds inhibited osteoclastogenesis. Taken together, BML endows biofunctionalized TCP scaffolds with the ability to inhibit osteoclast differentiation by activating the Wnt/β-catenin signaling pathway, ultimately exhibiting robust inhibitory effects on osteoclastic differentiation and functional activity.

Accumulating evidence has demonstrated that increased osteoclast activity disturbs remodeling of the osseous callus. Furthermore, osteoblastic bone formation may be impaired by swallowing Exos from activated osteoclasts [51]. Therefore, a proper strategy should focus on the balance of osteoblasts/osteoclasts. As mentioned in the previous sections, BML may act as a critical mediator in accelerating bone regeneration by promoting osteogenic differentiation and inhibiting osteoclastic differentiation. Previous studies also proved that BML could inhibit the differentiation and maturation of bone-resorbing osteoclasts by downregulating NFATc1 and CTSK through activating Wnt/β-catenin signaling [46]. The stimulation of NFATc1, a member of the transcription factor NFAT family and a crucial determinant of osteoclastogenesis, is associated with osteoclast differentiation and leads to the upregulation of several genes [52]. To further verify the effect of BML-loaded scaffolds on osteoclastogenesis, we then determined the expression of NFATc1, CTSK, RANK, TRAP, and DC-STAMP, which are all main regulatory factors of osteoclast formation and differentiation, in osteoclasts. As shown in Fig. 6D, the qRT–PCR assay results indicated that these genes in both the BP@TCP and SBP@TCP groups were significantly downregulated during culture compared with those in the other two groups. In particular, SBP@TCP suppressed the expression of all osteoclast-related genes more significantly than BP@TCP. NFATc1 and CTSK protein expression was further visualized using immunofluorescence staining. The results also demonstrated lower expression of NFATc1 and CTSK in the BP@TCP and SBP@TCP groups than in the P@TCP and TCP groups (Fig. 6E and F), which was consistent with the qRT–PCR assay. Moreover, a weaker fluorescence intensity of NFATc1 and CTSK staining was also observed, indicating the inhibition of osteoclast activity. Correspondingly, the relative fluorescence intensity of NFATc1 and CTSK staining for SBP@TCP was approximately 0.27 and 0.19, respectively, which was significantly lower than that in the other groups (Fig. S20). These data together suggested that the as-designed SBP@TCP scaffolds remarkably suppress the expression of osteoclastogenesis-related markers and dampen NFATc1-mediated osteoclastogenesis.

Studies have found that the regulatory function of the Wnt/β-catenin signaling pathway in osteoclast differentiation is mainly mediated by decreasing the expression of NFATc1 [46]. Given that, the Wnt/β-catenin signaling pathway was subsequently verified via western blot assay. As shown in Fig. 6G–H, β-catenin and GSK3β expression changed as expected. Of note, these findings are consistent with the results of osteogenic differentiation, further verifying the effective Wnt signaling activator of BML. Overall, all these results strongly supported that
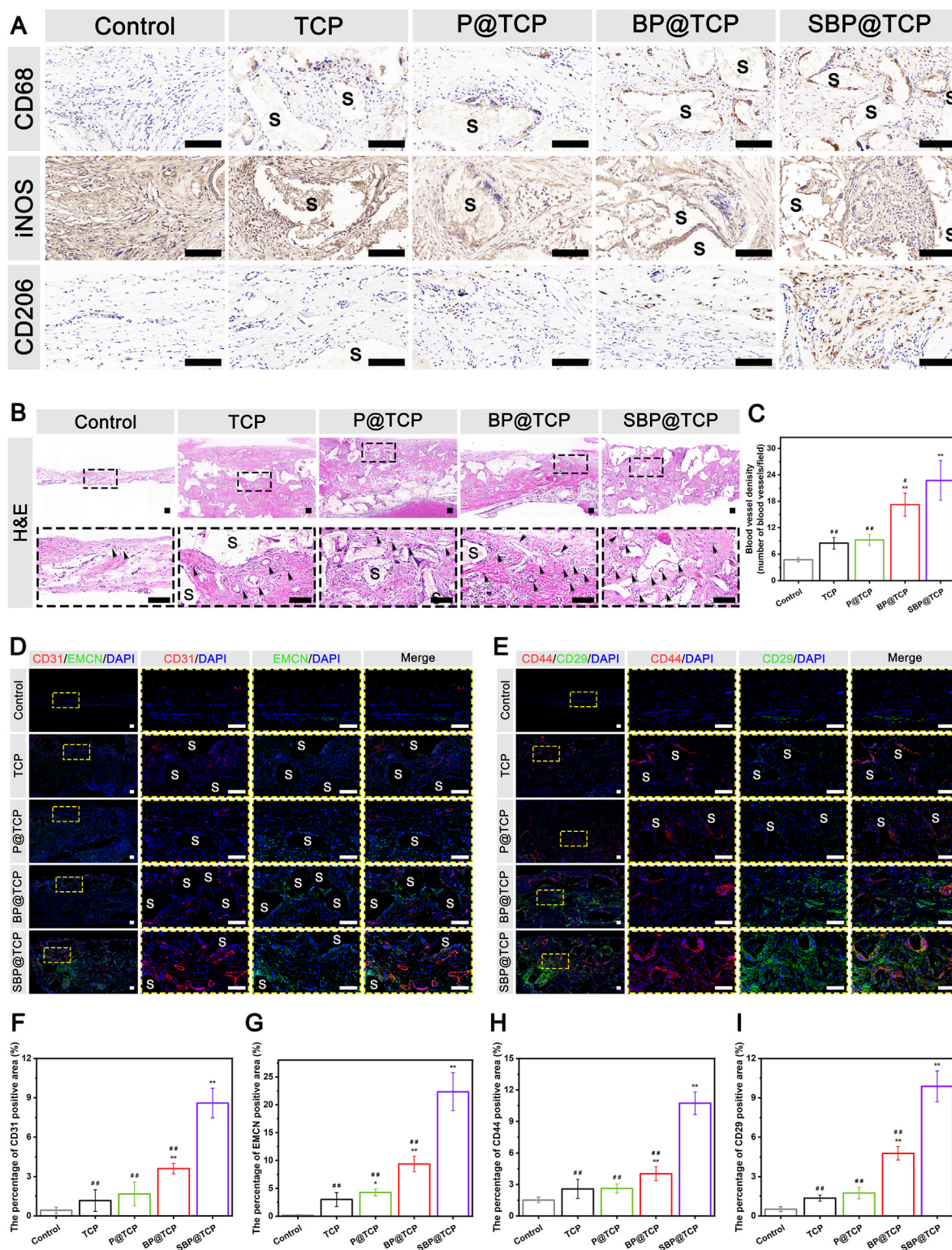
Fig. 7. In vivo immune response, neovascularization, and MSC recruitment. (**A**) Representative immunohistochemical staining images of CD68, iNOS, and CD206 in the defect area at 3 weeks after implantation. (**B**) Representative H&E staining images of the defect site. Black arrows indicate the newly formed blood vessels in the defect area. (**C**) Quantitative analysis of the average number of blood vessels. (**D**) Representative double-stained immunofluorescent staining images of CD31/EMCN and CD44/CD29 in the defect area. Scale bar: 100 μm (A, B, D). Data are presented as the mean ± SD (n = 3). *P < 0.05 and **P < 0.01 indicate significant differences compared with the control group. #P < 0.05 and # #P < 0.01 indicate significant differences compared with the SBP@TCP group.

BML-loaded TCP scaffolds activate the Wnt/β-catenin signaling pathway by inhibiting NFATc1 expression, thereby inhibiting osteoclast differentiation, which was partially consistent with previous studies [46]. Indeed, the activation of the classical Wnt/β-catenin pathway can

directly downregulate NFATc1 expression to inhibit the differentiation and maturation of osteoclasts, thereby affecting bone resorption [53]. On the other hand, former studies found that the activation of the Wnt/β-catenin pathway could indirectly inhibit osteoclastogenesis by

promoting the expression of OPG, which can competitively inhibit the binding between RANKL and RANK, thereby suppressing the formation and differentiation of osteoclasts [54]. Thus, BML-loaded scaffolds effectively activated the Wnt/β-catenin pathway, which downregulated the expression of NFATc1 and ultimately inhibited the formation of osteoclasts.

2.6. In vivo evaluation of the early immune response, vascularization, and MSC recruitment

Because immunomodulation and angiogenesis occur prior to the differentiation of the MSC-osteoblast lineage during the bone healing process, it is imperative to explore the osteoimmunomodulatory and angiogenic properties of fabricated scaffolds. Studies have shown that implantable biomaterials with favorable immune responses can guide successful osteogenesis and angiogenesis [5]. Encouraged by the aforementioned in vitro results, the in vivo immune responses of the scaffolds to the early local microenvironment were next investigated in calvarial defect models. It has been reported that the healing process of bone tissue begins with inflammation following immune cells, releasing inflammatory factors at the initial stage, consequently recruiting MSCs and guiding their osteogenic differentiation. This process is also closely related to neovascularization [55]. Therefore, the modulation of local immune responses following implantation is of great importance for bone regeneration. As the primary effector cells of nonspecific immunity, macrophages play a key role in orchestrating immunoinflammatory responses and tissue repair by releasing cytokines, growth factors, and chemokines to determine the fate of biomaterials [4]. In response to a variety of biophysical/biochemical signals, macrophages can be activated to a proinflammatory M1 phenotype, secreting inflammatory cytokines and participating as effector cells to resist intracellular pathogens, or an anti-inflammatory M2 phenotype, which has been found to take part in the alleviation of inflammation and the promotion of angiogenesis and tissue remodeling [56]. In particular, biomaterial-mediated regulation of macrophage polarization toward a balanced M1/M2 or predominantly M2 phenotype facilitated neovascularization, MSC recruitment, and osteogenesis, which could ensure successful long-term implantation in bone healing [5]. Thus, in this work, immunohistochemical staining of CD68 (panmacrophage marker), iNOS (M1 polarized marker), and CD206 (M2 polarized marker) was conducted in the early phase of the bone repair procedure (3 weeks after implantation). As shown in Fig. 7A, the expression of CD68 was significantly higher in all scaffold groups than in the empty control group, indicating that the porous structure of TCP-based scaffolds was beneficial to the inward migration of macrophages. In addition, the positive level of the M1 marker iNOS in the control and pure TCP groups was significantly higher than that in the three biofunctionalized scaffold groups, indicating a more active inflammatory response. The expression of iNOS in the SBP@TCP group was lower than that in the other groups, indicating a small number of M1 macrophages in the defect region. For the M2 marker CD206, the expression in the three biofunctionalized scaffold groups was higher than that in the pure TCP and control groups in the early stages. Notably, the SBP@TCP group showed the most abundant pro-healing M2-type macrophages (CD206-positive staining), followed by the BP@TCP and P@TCP groups, which implied a predominant M2 phenotype polarization of macrophages conducive to anti-inflammation and tissue repair induced by the SBP@TCP scaffold. This observation was also verified by an in vitro qRT–PCR assay (Fig. S21), which revealed that the typical M2 macrophage-related genes, including IL-4, IL-10, CD206, Arginase-1 (Arg-1), and transforming growth factor-β1 (TGF-β1), were significantly upregulated in the SBP@TCP group, indicating M2 macrophage activation. There is abundant evidence that timely termination of the proinflammatory response by optimizing the M1-to-M2 transition at the early stages of bone injury is a prerequisite for successful bone healing [57]. In the present study, our results suggested that BP@TCP and SBP@TCP have a good inhibitory effect on inflammation in

the relatively early stages of bone healing, which may be due to the presence of BML that could regulate the transition of M1 macrophages to M2 macrophages by activating the Wnt/β-catenin signaling pathway. Besides the role of BML, PDA, and CCS in SBP@TCP scaffolds may also participate in inducing M2 polarization of macrophages. Overall, the designed SBP@TCP scaffold can construct a pro-regenerative immune microenvironment by modulating the macrophage phenotype transition, which contributes to rapid vessel formation and bone regeneration in vivo.

After controlling inflammation, the subsequent phase of neovascularization and endogenous MSC recruitment should be activated. It is widely believed that accelerated angiogenesis is essential for tissue remodeling in the early stage of osteogenesis [50]. The in vitro angiogenesis results indicated that SBP@TCP could accelerate the migration, infiltration, and tube-forming function of HUVECs, as well as angiogenesis-related factor expression, revealing a strong ability to stimulate angiogenesis. However, whether this effect can be achieved in vivo remains unclear. To evaluate the ability of different scaffolds to induce in vivo angiogenesis, in this study, we carried out H&E staining of bone tissue slices at 3 weeks after surgery. As shown in Fig. 7B, there were markedly increased mature blood vessels around the BP@TCP and SBP@TCP scaffolds, and there were some blood capillaries in the pure P@TCP and P@TCP groups. In contrast, almost no neovascularization occurred in the empty control group. Quantitative analysis indicated that both the BP@TCP and SBP@TCP groups exhibited a greater number of blood vessels as well as vessels with a larger diameter in the defect area, especially in the SBP@TCP group (Fig. 7C). These results clearly demonstrated that SBP@TCP promoted angiogenesis and resulted in better microvessel ingrowth, which was possibly due to the presence of a Wnt signaling activator and an M2 macrophage-enriched regenerative microenvironment. A series of recent studies demonstrated that the specification of type H vessels unique to bone tissue could play an important role in bone regeneration. The coupling of angiogenesis and osteogenesis is tightly regulated by type H vessels, which are characterized by CD31 and EMCN double positivity [58]. Therefore, in this study, immunofluorescence staining of CD31 and EMCN was further used to observe type H capillary growth in the bone regeneration site. As shown in Fig. 7D, large quantities of type H capillaries (CD31$^+$ and EMCN$^+$, i.e., yellowish green areas) grew into the regeneration sites within the BML-loaded biofunctionalized scaffolds in vivo. Both the BP@TCP and SBP@TCP groups exhibited remarkably increased type H capillaries in the defect area, which had a significantly higher blood vessel density than the other groups. The highest enrichment of type H vessels was observed in the SBP@TCP group, followed by the BP@TCP and P@TCP groups, which is consistent with the results of H&E staining. In contrast, far fewer type H vessels developed in the control and pure TCP groups. Meanwhile, a higher percentage of CD31/EMCN-positive area was observed in the regenerated tissue implanted with BP@TCP and SBP@TCP scaffolds compared with the treatment of the other three scaffolds (Fig. 7F and G). These results suggested that the enhancement of early vascularization in SBP@TCP was mainly due to the synergistic effect of BML delivery and CCS modification, which is consistent with the in vitro results. It is known that the activation of Wnt/β-catenin signaling pathway can augment the proliferation of ECs by secreting VEGF, bFGF, and Ang-1 [59]. In addition, the SBP@TCP scaffold facilitated the tube formation of ECs such as HUVECs, which is consistent with the results obtained in vitro. Furthermore, the biological effect of scaffolds in promoting angiogenesis in a calvaria bone defect model is also regulated by the immune microenvironment in vivo. As mentioned earlier, this 3D biofunctionalized SBP@TCP scaffold can effectively induce the polarization of macrophages to the M2 phenotype, which promoted the expression of chemotactic and angiogenic factors, thereby accelerating EC migration toward the defect site to promote the maturation and remodeling of the vascular network. These effects together contributed to SBP@TCP-induced enhancement of angiogenesis in the bone defect area.

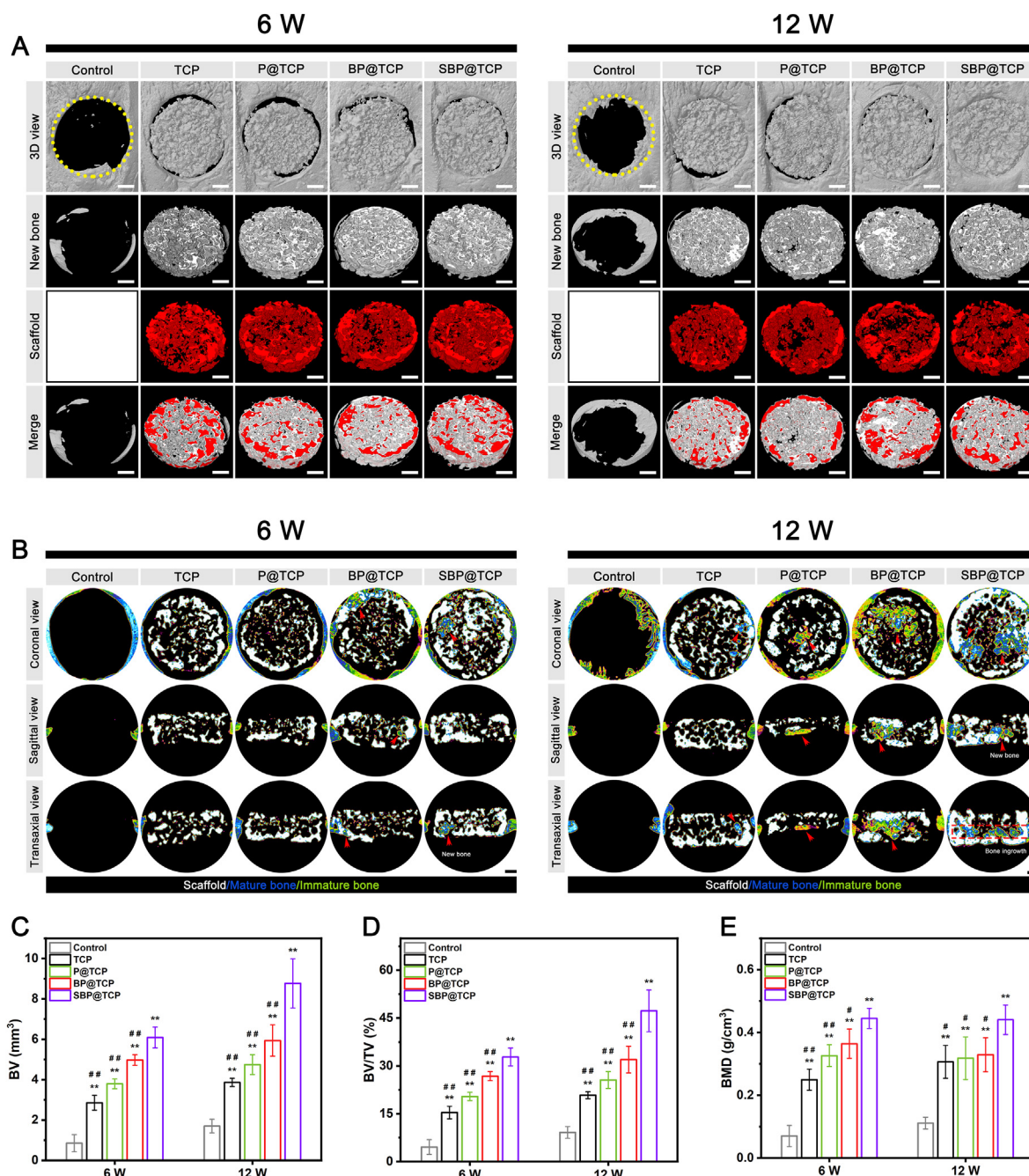In situ recruitment of endogenous MSCs is also a pivotal biological

Fig. 8. Radiological analysis of bone formation in vivo. (**A**) Representative 3D micro-CT images of calvarial defects at 6 and 12 weeks after implantation. Yellow dotted lines indicate the boundary of the defect (5 mm in diameter). (**B**) Newly formed bone tissue distribution in different groups at 6 and 12 weeks after implantation. (**C-E**) Quantitative analysis of micro-CT results of the newly formed bone tissue in the bone defect area, including BV, BV/TV, and BMD. Scale bar: 1 mm (A, B). Data are presented as the mean ± SD (n = 4). *P < 0.05 and **P < 0.01 indicate significant differences compared with the control group. #P < 0.05 and ##P < 0.01 indicate significant differences compared with the SBP@TCP group.

process in bone regeneration, which might accelerate subsequent osteogenesis of MSCs, neo-bone formation, and matrix mineralization [28]. After three weeks of implantation, the accumulative endogenous MSCs in bone tissue slices were identified by CD44/CD29 double immunofluorescence staining. As shown in Fig. 7E, few host cells with an MSC phenotype (CD29$^+$/CD44$^+$) appeared in the empty control and pure TCP groups, indicating poor MSC recruitment and infiltration in these groups. Conversely, more obvious positive expression of the CD29/CD44 marker was observed in SBP@TCP than in BP@TCP (Fig. 7H and I). Interestingly, a large number of CD29$^+$/CD44$^+$ cells were distributed around and within the pore wall of the SBP@TCP scaffold, implying that

the interconnected porous structure together with the BML-loaded bio-functionalized surface contributed to the fast recruitment of endogenous MSCs, which is essential for tissue regeneration and ingrowth. For regenerating bone defects, biomaterials with conducive MSC recruitment properties can modulate osteogenic differentiation, thereby enhancing bone regeneration by mimicking the endogenous microenvironment of native bone tissues. Numerous studies have revealed that macrophage infiltration into implanted biomaterials is closely related to the recruitment of osteoprogenitor cells in defects [60]. Consistently, our in vivo data confirmed the optimal capacity of SBP@TCP for facilitating rapid macrophage infiltration and M2 transition in rat cranial defects (Fig. 7A),
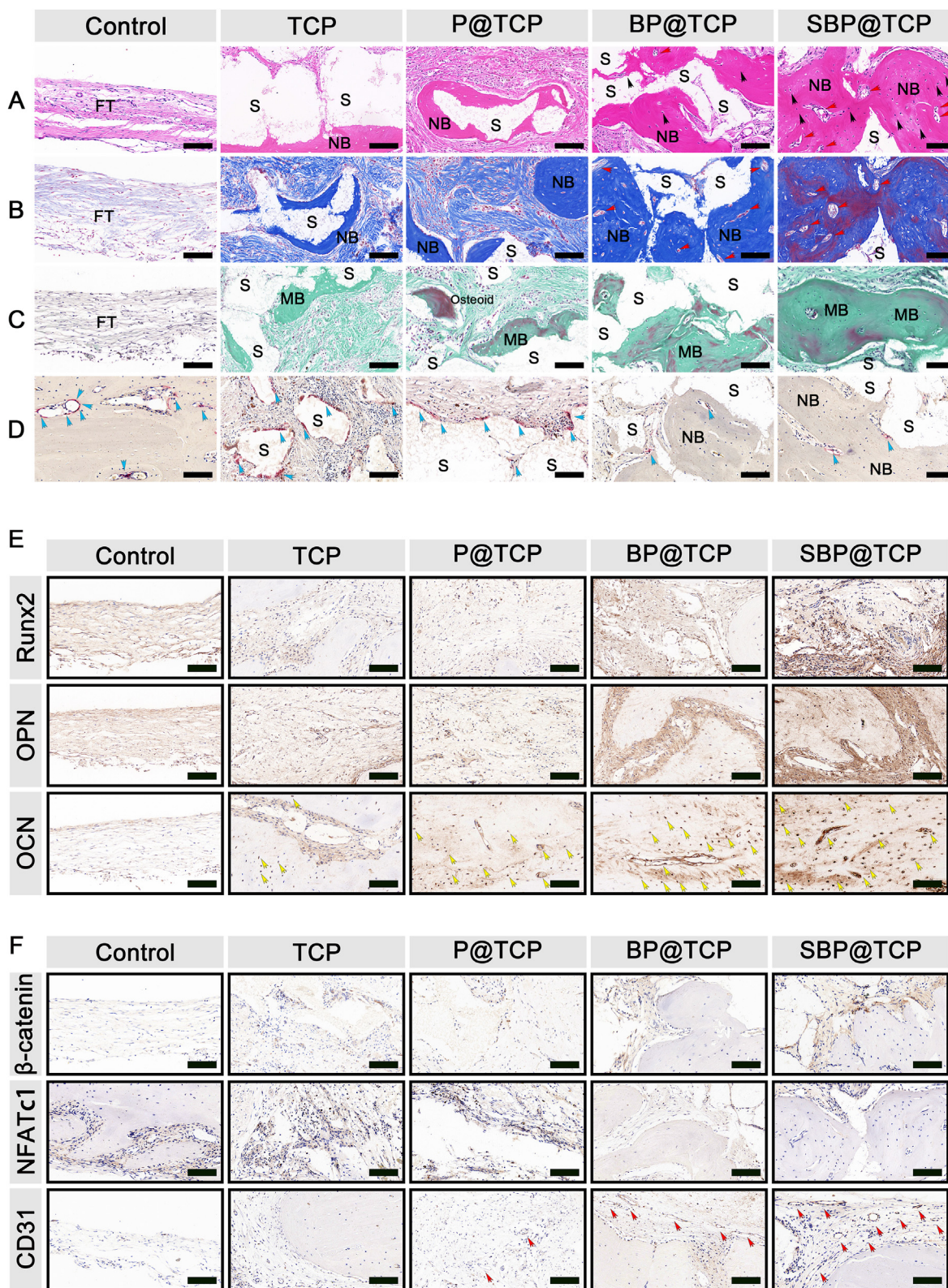
Fig. 9. Histological evaluation and immunohistochemical staining for bone regeneration and remodeling in the defect area with scaffold implantation. (**A-D**) Representative H&E staining, Masson's trichrome staining, and TRAP staining images at 12 weeks after implantation. (**E-F**) Representative immunohistochemical staining of osteogenesis (Runx2, OPN, OCN, β-catenin), osteoclastogenesis (NFATc1), and angiogenesis (CD31)-related markers at 12 weeks after implantation. Black arrows = bone lacunas; red arrows = central canals; yellow arrows = blood vessels; blue arrows = osteoclasts; S = residual scaffold; HB = host bone; NB = newly formed bone; FT = fibrous tissue; MB = mature/mineralized bone. Black asterisks: residual material. The green arrows indicate the target protein-positive zone in the defect areas. Scale bar: 100 μm (A–F).

which, in turn, would create an anti-inflammatory environment in the local injury site and release osteogenic factors, cytokines and chemokines to modulate the recruitment of critical cells (such as MSCs). Another important reason was associated with the stimulating effects of BML released from the SBP@TCP scaffold, which played a positive role in recruiting endogenous MSCs. Accordingly, we speculated that SBP@TCP could rapidly initiate angiogenesis and osteogenesis by in-situ recruitment of ESCs and subsequently accelerate osteo-differentiation to regenerate bone tissue after implantation in cranial defects. Taken together, these results are a good indication that BML-loaded scaffolds, especially SBP@TCP, had an enormous potential for recruiting CD29$^+$/CD44$^+$ cells (MSCs) within scaffolds, which creates an osteoinductive extracellular milieu that promotes host MSC recruitment and induces subsequent osteogenesis and neo-tissue mineralization.

2.7. In vivo evaluation of bone regeneration in rat calvarial defects

Given the superior cytocompatibility, pro-osteogenesis/angiogenesis and anti-osteoclastogenesis capacities, as well as the favorable immune responses of SBP@TCP, the in situ bone repair ability was further investigated. To determine the in vivo bone regeneration ability, biofunctionalized scaffolds were implanted in situ into critical-sized, 5 mm diameter cranial defects in rats (Fig. S22). The cranial bone defect model was established in rats according to a published procedure [60], and no severe complications occurred during the animal experiment. At 6 and 12 weeks postsurgery, bone regeneration in the defect site was evaluated by micro-CT and histological analysis. The consecutive micro-CT images revealed a dynamic and more precise bone repair process. As displayed in Fig. 8A, the 3D reconstructed micro-CT images demonstrated that all bone defects implanted with TCP-based scaffolds had various degrees of regenerated new bone formation after 6 and 12 weeks. In accordance with the expected results, there was more new bone growth for the BML-immobilized scaffolds than for those in the other groups, indicating the positive effect of BML on bone healing. It is worth noting that implantation of SBP@TCP achieved the best bone defect healing outcome and showed apparent bridging of the defect at 12 weeks. These results indicated that CCS and BML have a synergistic effect on accelerating new bone formation. Conversely, only a minimal amount of mineralized tissue was found in the empty control group, and most of the defects remained unhealed, which indicated that such a region could not self-repair, known as critical size. In addition, the 2D reconstruction images also proved that the newborn bone ingrowth and direct bone bonding in the SBP@TCP group were more pronounced than those in the BP@TCP and other groups, with a substantial amount of new bone tissue growing around and penetrating inside the SBP@TCP scaffolds (Fig. 8B). Specifically, the SBP@TCP group had the most significant quantity of mineralized bone tissues around and inside the scaffold. Coronal 2D micro-CT imaging showed that the newly formed bone tissue was closely connected, and some areas were connected to larger pieces and spread inside the scaffold along the 3D interconnected macropore channels. Moreover, transaxial 2D micro-CT imaging of the defect area displayed newborn bone tissue that had thoroughly grown across the defect in the SBP@TCP group. These results indicated that the SBP@TCP scaffolds could effectively guide bone regeneration by the synergistic effect of BML and CCS, providing a beneficial microenvironment for cell function and thus promoting bone healing. Then, BML regulates bone remodeling by activating the Wnt/β-catenin signaling pathway, which exerts a significant role in modulating osteoblast-mediated bone formation and osteoclast-mediated related bone resorption. Besides, we found that the pure TCP and P@TCP scaffolds did not exhibit satisfactory bone regeneration. This result demonstrates that, in the absence of osteogenic induction cues, the TCP and P@TCP scaffolds only served as a barrier to offer space for osteogenesis without sufficient osteoinductivity, but this effect was limited in the critical-sized cranial bone defect model of SD rats, consistent with the results reported in previous studies [61]. The residual TCP-based scaffolds could also be observed by 2D and 3D micro-CT reconstruction

images. As the implantation time increased, these scaffolds gradually degraded but still maintained the integrity of the internal pore structure at 12 weeks. This phenomenon indicated that the degradation rate of these scaffolds could meet the requirement of guided bone regeneration, which facilitated cell infiltration and tissue replacement during the process of bone repair. Meanwhile, with the ingrowth of newborn bone tissue, the SBP@TCP scaffold was obviously absorbed, and fragments were observed in the mineralized matrix spacing, indicating the favorable biodegradability of the SBP@TCP scaffold. Quantitative analysis of bone morphological parameters, including BV, BV/TV, and BMD, further confirms the above findings. As depicted in Fig. 8C–E, the levels of BV, BV/TV, and BMD in both the BP@TCP and SBP@TCP scaffold groups were significantly higher than those of the other three groups and were highest in the SBP@TCP group at both 6 weeks and 12 weeks, which meant that the SBP@TCP scaffold possessed the quickest and best bone-forming bioactivity to favor bone formation. These results indicate that the TCP-based scaffolds can enhance bone formation in vivo. The introduction of BML and CCS may facilitate bone formation, with positive synergistic effects observed for the SBP@TCP scaffold.

Histological analysis was conducted to further evaluate the bone formation pattern in the defect sites at 12 weeks after implantation. As displayed in Fig. 9A, the results of H&E staining indicated that only a thin layer of fibrous tissue was formed in the empty control group, with a small amount of calcified tissue developed at the peripheral region. This was indicative that without the support of a scaffold, new bone tissue formation was hardly achieved in a critical-sized cranial bone defect. For the pure TCP and P@TCP groups, the bone defect region was mostly covered with undegraded material and scattered localized immature woven bone without integral bridging in the defect site, indicating that the appropriate pore size and interconnected porous structure in the scaffold had a certain beneficial effect on bone regeneration. However, extensive newborn bone tissue was developed around the pore channels in the BP@TCP and SBP@TCP groups, especially in the SBP@TCP group, with bone structure and bone mineralization comparable to the surrounding native bone tissue. Notably, the newly formed bone tissues almost filled every corner of the scaffold, including the center and the edges, detected not only at the surrounding but also in the center area of the SBP@TCP scaffolds, which was also indicative of sustained release of BML and CCS modification, synergistically promoting MSC recruitment, osteogenic differentiation, and subsequent mineralization inside the scaffold and finally shortening the bone repair time. These results were in accordance with the micro-CT data.

Further Masson's trichrome staining indicated that conspicuously more mature neo-bone (colored red) was found in the SBP@TCP group than in the BP@TCP group (Fig. 9B). The latter evidently had many more blue-stained areas, indicating immature collagen fibers and osteoids. On the other hand, the defect region in the P@TCP and TCP groups was filled with a large amount of collagen fibrils, fibrous tissues, and sporadically distributed immature bone tissues (colored in blue), while that in the empty control group remained vacant and was partly covered with densely arranged fibers. These staining results also revealed that more newly formed bone lacunae (labeled as black arrows) and central canals (labeled as red arrows) were developed in the regenerated bone tissues of the SBP@TCP group, further verifying the enhanced osteogenic and angiogenic potential. These observations verified that bone defect repair was enhanced and accelerated in both the BP@TCP and SBP@TCP groups compared with the other groups, and the SBP@TCP group showed better healing characteristics than the other groups, which was in accordance with the expected results.

In vivo bone mineralization and bone resorption were further investigated via Goldner's trichrome staining (Fig. 9C) and TRAP staining (Fig. 9D), respectively. As expected, a large amount of mineralized bone in dark green together with few TRAP-positive osteoclasts was observed in the defect area of the BP@TCP and SBP@TCP groups, especially in the SBP@TCP group, which confirmed that the SBP@TCP scaffold promotes the maturation of new bone while suppressing bone resorption during
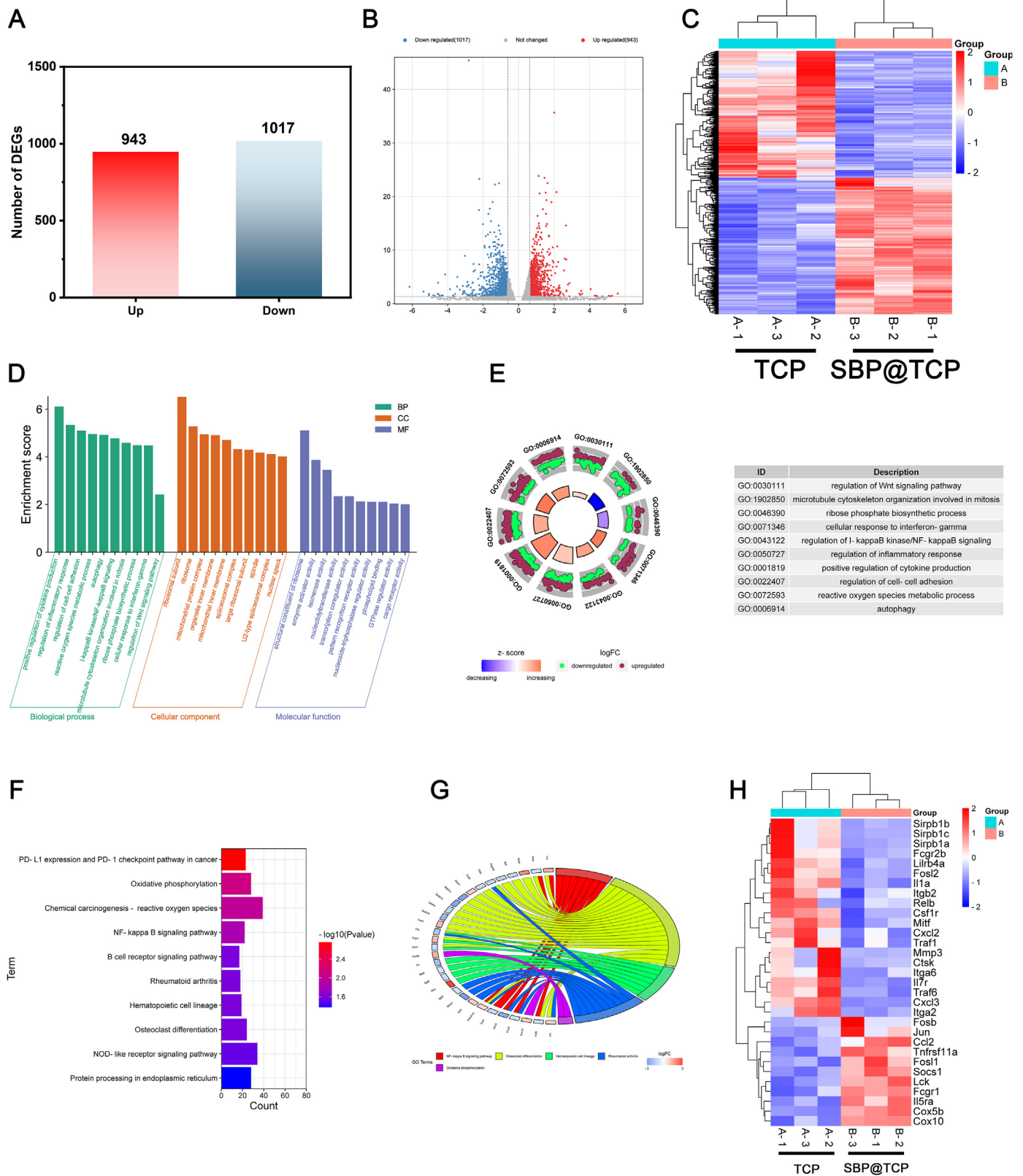
Fig. 10. Results of transcriptome sequencing. (**A**) The number of upregulated (red) and downregulated genes (blue). (**B**) Volcano plot of RNA-seq data of BMMs in SBP@TCP and TCP. (**C**) Heatmap of differentially expressed genes (DEGs) for BMMs in SBP@TCP and TCP. (**D**) GOBubble plot of GO enrichment analysis in DEGs. (**E**) GOCircle plot of GO enrichment analysis of the DEGs. (**F**) GOBubble plot of KEGG enrichment analysis in DEGs. (**G**) GOchord of KEGG enrichment analysis of DEGs, including "Osteoclast differentiation", "Rheumatoid arthritis", "Hematopoietic cell lineage", "NF-kappa B signaling pathway", and "Oxidative phosphorylation". (**H**) Heatmap of DEGs for BMMs in GOchord of KEGG enrichment analysis.

bone repair. In contrast, sparse immature bone (osteoid, stained orange/red) and many osteoclasts (stained claret) were detected in all other groups at 12 weeks after implantation. These results suggested that BML-loaded biofunctionalized scaffolds could serve as favorable candidates for osteoblast/osteoclast differentiation regulation, thereby exerting a synergistic effect on accelerating bone regeneration and remodeling.

To explain the underlying mechanisms of BML-loaded TCP scaffold-mediated osteogenesis and anti-osteoclastogenesis, immunohistochemical analyses of Runx2, OPN, OCN, β-catenin, and NFATc1 were performed at 12 weeks. As shown in Fig. 9E and F, higher osteogenesis-related expression of Runx2, OPN, and OCN in the BP@TCP and SBP@TCP groups was verified. Significantly, the SBP@TCP group had more patches of brown and/or reddish-brown staining areas than all other groups, implying mature bone-specific ECM deposition and mineralization. In contrast, there were few positive staining areas in the defect region of the empty control group, which were primarily filled with fibrous connective tissues. The better bone formation in the SBP@TCP group could be attributed to the synergistic effect of BML delivery and CCS modification facilitating the ingrowth of blood vessels and bone tissues within the SBP@TCP scaffolds and thereby effectively promoting the quality and rate of bone reconstruction. Studies have shown that the expression of osteogenesis-related markers, such as ALP, Runx2, and OPN, is beneficial for the regeneration of bone defects and bone healing [62]. Simultaneously, the analysis and statistics of β-catenin and NFATc1 further supported the effects of BML-loaded TCP scaffolds on bone resorption via inhibition of NFATc1 activity via Wnt stimulation, which allows β-catenin to accumulate in the cytoplasm and enter the nucleus. These in vivo immunohistochemical analyses yielded results that were similar to those obtained by in vitro assays, suggesting the beneficial effect of SBP@TCP on bone regeneration via activation of the Wnt/β-catenin signaling pathway.

To assess the formation of blood vessels in the bone defect area, decalcified bone tissue samples were further processed with immunohistochemical staining of CD31, a typical marker for vascular ECs. As shown in Fig. 9F, bone defects treated with pure TCP and the control groups showed extremely low positive expression with only a few blood vessels. However, due to the optimized biofunctionalization, both the BP@TCP and SBP@TCP groups exhibited remarkably increased CD31-positive staining in the defect area, which had a higher blood vessel density than the other groups. In addition, the synergistic effect of BML and CCS modification conferred SBP@TCP with robust stimulation of vascularized bone regeneration, with evident infiltration of blood vessels (red arrows) in the defect area. The higher positive expression level of CD31 in SBP@TCP implied a greater potential for accelerating vascularization. It has been reported that blood vessel formation can facilitate communication among pores, thus promoting angiogenesis and osteogenesis [63]. To evaluate the long-term toxicity of these biofunctionalized TCP scaffolds in vivo, H&E staining of the major organs of rats, including the heart, liver, spleen, lung, and kidney, was performed 12 weeks after surgery. No significant pathological change was found in any group (Fig. S23), which implies that the 3D biofunctionalized TCP scaffolds are biocompatible and will not cause local or systemic toxicity. Based on our radiological and histological examinations, BML-loaded biofunctionalized TCP scaffolds, especially the SBP@TCP scaffold, can accelerate the healing of bone defects by promoting the deposition of bone-specific proteins and the generation of new blood vessels, which could serve as an effective and promising material for promoting bone tissue regeneration.

To dissect the mechanism by which SBP@TCP inhibits osteoclast differentiation, we performed transcriptomic RNA sequencing (RNA-seq). As shown in Fig. 10A–C, volcano and heatmap analysis identified 1960 differentially expressed genes in the BMMs of the SBP@TCP scaffold group, of which 943 genes were upregulated and 1017 genes were downregulated. Gene Ontology (GO) analysis revealed that SBP@TCP altered biological processes, cellular components, and molecular functions, with significant enrichment of genes related to the Wnt signaling

pathway, I-kappaB kinase/NF-kappaB signaling, cytokine production and inflammatory response (Fig. 10 D-E). Moreover, KEGG analysis revealed a significant enrichment of genes related to Oxidative phosphorylation, Rheumatoid arthritis, Osteoclast differentiation, Chemical carcinogenesis - reactive oxygen species, the NOD-like receptor signaling pathway and the NF-kappa B signaling pathway (Fig. 10F). In addition, GOChord was used to further analyze the enrichment project related to osteoclasts in vivo. The enriched genes were assigned to the following categories: "Osteoclast differentiation", "NF-kappa B signaling pathway", "Rheumatoid arthritis", "Oxidative phosphorylation", and "Hematopoietic cell lineage" (Fig. 10G). Furthermore, heatmap analysis defined the differential expression of enriched genes in SBP@TCP-treated BMMs (Fig. 10H). These data were in accordance with the above in vitro study, demonstrating that SBP@TCP is capable of regulating the expression of osteoclast differentiation genes.

3. Conclusion

In summary, a novel biofunctionalized 3D SBP@TCP scaffold with appropriate physicochemical properties was successfully fabricated via a combination of bioinspired dopamine chemistry and a self-assembly strategy for enhanced bone defect healing. The pure TCP scaffold, as a macroscopic framework, provided mechanical support and inorganic components, while the BML-loaded sandwich-like hybrid surface conferred bioactive properties, such as cell adhesion, proliferation, and differentiation, through the stable and long-term sustained release of BML. The results of in vitro cell experiments demonstrated that SBP@TCP possesses remarkably pro-osteogenic, pro-angiogenic, and anti-osteoclastic capabilities based on its ability to effectively activate the Wnt/β-catenin signaling pathway. Significantly, in vivo bone defect repair assessment further mirrored the aforementioned results and verified that the transplantation of the biofunctionalized TCP scaffold induced favorable osteogenesis and angiogenesis while deactivating osteoclastogenesis, ultimately accelerating in situ bone regeneration. Thus, this multifunctional TCP implant is well suited for orthopedic applications. Moreover, this work provides a green, facile, and low-cost surface modification strategy, and the remarkable biological functions achieved by smart cell-instructive TCP implants hold great potential for clinical translation.

CRediT author statement

Minhao Wu, **Feixiang Chen**, and **Huifan Liu** contributed equally to this work. **Yufeng Zhang**: Conceptualization, Methodology, Investigation, Writing-original draft, Project administration. **Feixiang Chen**: Conceptualization, Methodology, Investigation, Writing-original draft. **Huifan Liu**: Conceptualization, Methodology, Investigation, Writing-original draft. **Ping Wu**: Investigation. **Zhiqiang Yang**: Investigation. **Zhe Zhang**: Investigation. **Jiajia Su**: Methodology, Writing-original draft, Supervision. **Lin Cai**: Conceptualization, Methodology, Writing-original draft, Supervision. **Yufeng Zhang**: Conceptualization, Methodology, Writing-original draft, Supervision, Funding acquisition.

Declaration of competing interest

The authors declare that they have no known competing financial interests or personal relationships that could have appeared to influence the work reported in this paper.

Data availability

Data will be made available on request.

Appendix A. Supplementary data

Supplementary data to this article can be found online at https://doi.org/10.1016/j.mtbio.2022.100458.

References

[1] J. Huang, D. Lin, Z. Wei, Q. Li, J. Zheng, Q. Zheng, L. Cai, X. Li, Y. Yuan, J. Li, Parathyroid hormone derivative with reduced osteoclastic activity promoted bone regeneration via synergistic bone remodeling and angiogenesis, Small 16 (6) (2020), e1905876.

[2] C.-S. Lee, H.S. Hwang, S. Kim, J. Fan, T. Aghaloo, M. Lee, Inspired by nature: facile design of nanoclay–organic hydrogel bone sealant with multifunctional properties for robust bone regeneration, Adv. Funct. Mater. 30 (43) (2020), 2003717.

[3] W. Chen, G. Xie, Y. Lu, J. Wang, B. Feng, Q. Wang, K. Xu, J. Bao, An improved osseointegration of metal implants by pitavastatin loaded multilayer films with osteogenic and angiogenic properties, Biomaterials 280 (2022), 121260.

[4] S. Huo, F. Wang, Z. Lyu, Q. Hong, B.e. Nie, J. Wei, Y. Wang, J. Zhang, B. Yue, Dual-functional polyetheretherketone surface modification for regulating immunity and bone metabolism, Chem. Eng. J. 426 (2021), 130806.

[5] L. Bai, P. Chen, R. Hang, X. Yao, B. Tang, C. Liu, Y. Xiao, R. Hang, A micro/nano-biomimetic coating on titanium orchestrates osteo/angio-genesis and osteoimmunomodulation for advanced osseointegration, Biomaterials 278 (2021), 121162.

[6] M. Lian, B. Sun, Y. Han, B. Yu, W. Xin, R. Xu, B. Ni, W. Jiang, Y. Hao, X. Zhang, Y. Shen, Z. Qiao, K. Dai, A low-temperature-printed hierarchical porous sponge-like scaffold that promotes cell-material interaction and modulates paracrine activity of MSCs for vascularized bone regeneration, Biomaterials 274 (2021), 120841.

[7] J. Bai, H. Wang, H. Chen, G. Ge, M. Wang, A. Gao, L. Tong, Y. Xu, H. Yang, G. Pan, P.K. Chu, D. Geng, Biomimetic osteogenic peptide with mussel adhesion and osteoimmunomodulatory functions to ameliorate interfacial osseointegration under chronic inflammation, Biomaterials 255 (2020), 120197.

[8] S. Jin, Z. Gao, R. Yang, C. Yuan, R. Wang, Q. Zou, Y. Zuo, M. Zhu, Y. Li, Y. Man, J. Li, A baicalin-loaded coaxial nanofiber scaffold regulated inflammation and osteoclast differentiation for vascularized bone regeneration, Bioact. Mater. 8 (2022) 559–572.

[9] L. Cheng, Z. Chen, Z. Cai, J. Zhao, M. Lu, J. Liang, F. Wang, J. Qi, W. Cui, L. Deng, Bioinspired functional black phosphorus electrospun fibers achieving recruitment and biomineralization for staged bone regeneration, Small 16 (50) (2020), e2005433.

[10] H. Li, H. Wang, J. Pan, J. Li, K. Zhang, W. Duan, H. Liang, K. Chen, D. Geng, Q. Shi, H. Yang, B. Li, H. Chen, Nanoscaled bionic periosteum orchestrating the osteogenic microenvironment for sequential bone regeneration, ACS Appl. Mater. Interfaces 12 (33) (2020) 36823–36836.

[11] X. Xu, M. Sun, D. Wang, W. Bu, Z. Wang, Y. Shen, K. Zhang, D. Zhou, B. Yang, H. Sun, Bone formation promoted by bone morphogenetic protein-2 plasmid-loaded porous silica nanoparticles with the involvement of autophagy, Nanoscale 11 (45) (2019) 21953–21963.

[12] M.M. Hasani-Sadrabadi, P. Sarrion, N. Nakatsuka, T.D. Young, N. Taghdiri, S. Ansari, T. Aghaloo, S. Li, A. Khademhosseini, P.S. Weiss, A. Moshaverinia, Hierarchically patterned polydopamine-containing membranes for periodontal tissue engineering, ACS Nano 13 (4) (2019) 3830–3838.

[13] S.S. Lee, J.H. Kim, J. Jeong, S.H.L. Kim, R.H. Koh, I. Kim, S. Bae, H. Lee, N.S. Hwang, Sequential growth factor releasing double cryogel system for enhanced bone regeneration, Biomaterials 257 (2020), 120223.

[14] M. Li, T. Yu, J. Lai, X. Han, J. Hu, Z. Deng, D. Li, Z. Ye, S. Wang, C. Hu, X. Xu, Ethoprophos induces cardiac toxicity in zebrafish embryos, Ecotoxicol. Environ. Saf. 228 (2021), 113029.

[15] C. Liu, L. Chen, W. Wang, D. Qin, C. Jia, M. Yuan, H. Wang, Y. Guo, J. Zhu, Y. Zhou, H. Zhao, T. Liu, Emodin suppresses the migration and invasion of melanoma cells, Biol. Pharmaceut. Bull. 44 (6) (2021) 771–779.

[16] H. Li, L. Li, Y. He, W. Mao, H. Ni, A. Wang, F. Lyu, Y. Dong, Wnt/β-Catenin pathway balances scaffold degradation and bone formation in tissue-engineered laminae, Stem Cell. Int. 2021 (2021), 8359582.

[17] K.D. Hankenson, K. Gagne, M. Shaughnessy, Extracellular signaling molecules to promote fracture healing and bone regeneration, Adv. Drug Deliv. Rev. 94 (2015) 3–12.

[18] F. Wu, B. Li, X. Hu, F. Yu, Y. Shi, L. Ye, Wnt7b inhibits osteoclastogenesis via AKT activation and glucose metabolic rewiring, Front. Cell Dev. Biol. 9 (2021), 771336.

[19] X. Xing, S. Han, Y. Ni, G. Cheng, Y. Cheng, X. Ni, Y. Deng, Z. Li, Z. Li, Mussel-inspired functionalization of electrospun scaffolds with polydopamine-assisted immobilization of mesenchymal stem cells-derived small extracellular vesicles for enhanced bone regeneration, Int. J. Pharm. 609 (2021), 121136.

[20] Y. Xue, W. Niu, M. Wang, M. Chen, Y. Guo, B. Lei, Engineering a biodegradable multifunctional antibacterial bioactive nanosystem for enhancing tumor photothermo-chemotherapy and bone regeneration, ACS Nano 14 (1) (2020) 442–453.

[21] Y. Qian, X. Zhou, F. Zhang, T.G.H. Diekwisch, X. Luan, J. Yang, Triple PLGA/PCL scaffold modification including silver impregnation, collagen coating, and electrospinning significantly improve biocompatibility, antimicrobial, and osteogenic properties for orofacial tissue regeneration, ACS Appl. Mater. Interfaces 11 (41) (2019) 37381–37396.

[22] X. Zhao, L. Zhou, Q. Li, Q. Zou, C. Du, Biomimetic mineralization of carboxymethyl chitosan nanofibers with improved osteogenic activity in vitro and in vivo, Carbohydr. Polym. 195 (2018) 225–234.

[23] Y. Yan, H. Chen, H. Zhang, C. Guo, K. Yang, K. Chen, R. Cheng, N. Qian, N. Sandler, Y.S. Zhang, H. Shen, J. Qi, W. Cui, L. Deng, Vascularized 3D printed scaffolds for promoting bone regeneration, Biomaterials 190–191 (2019) 97–110.

[24] S. Cheng, D. Zhang, M. Li, X. Liu, Y. Zhang, S. Qian, F. Peng, Osteogenesis, angiogenesis and immune response of Mg-Al layered double hydroxide coating on pure Mg, Bioact. Mater. 6 (1) (2021) 91–105.

[25] Z. Yang, Y. Xi, J. Bai, Z. Jiang, S. Wang, H. Zhang, W. Dai, C. Chen, Z. Gou, G. Yang, C. Gao, Covalent grafting of hyperbranched poly-L-lysine on Ti-based implants achieves dual functions of antibacteria and promoted osseointegration in vivo, Biomaterials 269 (2021), 120534.

[26] W. Cheng, X. Zeng, H. Chen, Z. Li, W. Zeng, L. Mei, Y. Zhao, Versatile polydopamine platforms: synthesis and promising applications for surface modification and advanced nanomedicine, ACS Nano 13 (8) (2019) 8537–8565.

[27] G.L. Koons, M. Diba, A.G. Mikos, Materials design for bone-tissue engineering, Nat. Rev. Mater. 5 (8) (2020) 584–603.

[28] S.J. Wang, D. Jiang, Z.Z. Zhang, Y.R. Chen, Z.D. Yang, J.Y. Zhang, J. Shi, X. Wang, J.K. Yu, Biomimetic nanosilica-collagen scaffolds for in situ bone regeneration: toward a cell-free, one-step surgery, Adv. Mater. (Deerfield Beach, Fla.) 31 (49) (2019), e1904341.

[29] K. Zhou, P. Yu, X. Shi, T. Ling, W. Zeng, A. Chen, W. Yang, Z. Zhou, Hierarchically porous hydroxyapatite hybrid scaffold incorporated with reduced graphene oxide for rapid bone ingrowth and repair, ACS Nano 13 (8) (2019) 9595–9606.

[30] R. Zhang, L. Deng, J. Guo, H. Wang, L. Zhang, X. Cao, A. Yu, B. Duan, Solvent mediating the in situ self-assembly of polysaccharides for 3D printing biomimetic tissue scaffolds, ACS Nano 15 (11) (2021) 17790–17803.

[31] T. Zhu, Y. Cui, M. Zhang, D. Zhao, G. Liu, J. Ding, Engineered three-dimensional scaffolds for enhanced bone regeneration in osteonecrosis, Bioact. Mater. 5 (3) (2020) 584–601.

[32] L. Zhang, G. Yang, B.N. Johnson, X. Jia, Three-dimensional (3D) printed scaffold and material selection for bone repair, Acta Biomater. 84 (2019) 16–33.

[33] T. Zhu, M. Jiang, M. Zhang, L. Cui, X. Yang, X. Wang, G. Liu, J. Ding, X. Chen, Biofunctionalized composite scaffold to potentiate osteoconduction, angiogenesis, and favorable metabolic microenvironment for osteonecrosis therapy, Bioact. Mater. 9 (2022) 446–460.

[34] T. Xiao, L. Fan, R. Liu, X. Huang, S. Wang, L. Xiao, Y. Pang, D. Li, J. Liu, Y. Min, Fabrication of dexamethasone-loaded dual-metal-organic frameworks on polyetheretherketone implants with bacteriostasis and angiogenesis properties for promoting bone regeneration, ACS Appl. Mater. Interfaces 13 (43) (2021) 50836–50850.

[35] X. Liu, M. Chen, J. Luo, H. Zhao, X. Zhou, Q. Gu, H. Yang, X. Zhu, W. Cui, Q. Shi, Immunopolarization-regulated 3D printed-electrospun fibrous scaffolds for bone regeneration, Biomaterials 276 (2021), 121037.

[36] C. Zhou, S. Liu, J. Li, K. Guo, Q. Yuan, A. Zhong, J. Yang, J. Wang, J. Sun, Z. Wang, Collagen functionalized with graphene oxide enhanced biomimetic mineralization and in situ bone defect repair, ACS Appl. Mater. Interfaces 10 (50) (2018) 44080–44091.

[37] Y. Yang, Q. Zhang, T. Xu, H. Zhang, M. Zhang, L. Lu, Y. Hao, J.H. Fuh, X. Zhao, Photocrosslinkable nanocomposite ink for printing strong, biodegradable and bioactive bone graft, Biomaterials 263 (2020), 120378.

[38] Y. Jiang, W. Wang, X. Wu, J. Shi, Pizotifen inhibits the proliferation and invasion of gastric cancer cells, Exp. Ther. Med. 19 (2) (2020) 817–824.

[39] C. Ji, M. Qiu, H. Ruan, C. Li, L. Cheng, J. Wang, C. Li, J. Qi, W. Cui, L. Deng, Transcriptome analysis revealed the symbiosis niche of 3D Scaffolds to accelerate bone defect healing, Adv. Sci. (Weinheim, Baden-Wurttemberg, Germany) (2022), e2105194.

[40] J. Long, W. Zhang, Y. Chen, B. Teng, B. Liu, H. Li, Z. Yao, D. Wang, L. Li, X.F. Yu, L. Qin, Y. Lai, Multifunctional magnesium incorporated scaffolds by 3D-Printing for comprehensive postsurgical management of osteosarcoma, Biomaterials 275 (2021), 120950.

[41] C. Wang, W.W. Lu, M. Wang, Multifunctional fibrous scaffolds for bone regeneration with enhanced vascularization, J. Mater. Chem. B 8 (4) (2020) 636–647.

[42] X. Liu, L. Li, B. Gaihre, S. Park, Y. Li, A. Terzic, B.D. Elder, L. Lu, Scaffold-free spheroids with two-dimensional heteronano-layers (2DHNL) enabling stem cell and osteogenic factor codelivery for bone repair, ACS Nano 16 (2) (2022) 2741–2755.

[43] Y. Liu, Z. Zhu, X. Pei, X. Zhang, X. Cheng, S. Hu, X. Gao, J. Wang, J. Chen, Q. Wan, ZIF-8-Modified multifunctional bone-adhesive hydrogels promoting angiogenesis and osteogenesis for bone regeneration, ACS Appl. Mater. Interfaces 12 (33) (2020) 36978–36995.

[44] M. Zhang, R. Lin, X. Wang, J. Xue, C. Deng, C. Feng, H. Zhuang, J. Ma, C. Qin, L. Wan, J. Chang, C. Wu, 3D printing of Haversian bone-mimicking scaffolds for multicellular delivery in bone regeneration, Sci. Adv. 6 (12) (2020) eaaz6725.

[45] M. Wu, F. Chen, P. Wu, Z. Yang, S. Zhang, L. Xiao, Z. Deng, C. Zhang, Y. Chen, L. Cai, Nanoclay mineral-reinforced macroporous nanocomposite scaffolds for in situ bone regeneration: in vitro and in vivo studies, Mater. Des. 205 (2021), 109734.

[46] X. Sun, K. Li, M. Hase, R. Zha, Y. Feng, B.Y. Li, H. Yokota, Suppression of breast cancer-associated bone loss with osteoblast proteomes via Hsp90ab1/moesin-

mediated inhibition of TGFβ/FN1/CD44 signaling, Theranostics 12 (2) (2022) 929–943.

[47] H. Shan, X. Zhou, B. Tian, C. Zhou, X. Gao, C. Bai, B. Shan, Y. Zhang, S. Sun, D. Sun, Q. Fan, X. Zhou, C. Wang, J. Bai, Gold nanorods modified by endogenous protein with light-irradiation enhance bone repair via multiple osteogenic signal pathways, Biomaterials 284 (2022), 121482.

[48] L.J. Qiao, K.L. Kang, J.S. Heo, Simvastatin promotes osteogenic differentiation of mouse embryonic stem cells via canonical Wnt/β-catenin signaling, Mol. Cell. 32 (5) (2011) 437–444.

[49] J. Wang, J. Lin, L. Chen, L. Deng, W. Cui, Endogenous electric-field-coupled electrospun short fiber via collecting wound exudation, Adv. Mater. (Deerfield Beach, Fla.) 34 (9) (2022), e2108325.

[50] D.S. Kim, J.K. Lee, J.H. Kim, J. Lee, D.S. Kim, S. An, S.B. Park, T.H. Kim, J.S. Rim, S. Lee, D.K. Han, Advanced PLGA hybrid scaffold with a bioactive PDRN/BMP2 nanocomplex for angiogenesis and bone regeneration using human fetal MSCs, Sci. Adv. 7 (50) (2021), eabj1083.

[51] B. Mi, L. Chen, Y. Xiong, Y. Yang, A.C. Panayi, H. Xue, Y. Hu, C. Yan, L. Hu, X. Xie, Z. Lin, W. Zhou, F. Cao, X. Xiao, Q. Feng, G. Liu, Osteoblast/osteoclast and immune cocktail therapy of an exosome/drug delivery multifunctional hydrogel accelerates fracture repair, ACS Nano 16 (1) (2022) 771–782.

[52] W. Gu, Z. Wang, Z. Sun, Z. Bao, L. Zhang, Y. Geng, L. Jing, X. Mao, L. Li, Role of NFATc1 in the bone-vascular Axis calcification paradox, J. Cardiovasc. Pharmacol. 75 (3) (2020) 200–207.

[53] M.M. Weivoda, M. Ruan, C.M. Hachfeld, L. Pederson, A. Howe, R.A. Davey, J.D. Zajac, Y. Kobayashi, B.O. Williams, J.J. Westendorf, S. Khosla, M.J. Oursler, Wnt signaling inhibits osteoclast differentiation by activating canonical and noncanonical cAMP/PKA pathways, J. Bone Miner. Res. : Off. J. Am. Soc. Bone Min. Res. 31 (1) (2016) 65–75.

[54] S. Minear, P. Leucht, J. Jiang, B. Liu, A. Zeng, C. Fuerer, R. Nusse, J.A. Helms, Wnt proteins promote bone regeneration, Sci. Transl. Med. 2 (29) (2010), 29ra30.

[55] Y. Li, L. Yang, Y. Hou, Z. Zhang, M. Chen, M. Wang, J. Liu, J. Wang, Z. Zhao, C. Xie, X. Lu, Polydopamine-mediated graphene oxide and nanohydroxyapatite-incorporated conductive scaffold with an immunomodulatory ability accelerates periodontal bone regeneration in diabetes, Bioact. Mater. 18 (2022) 213–227.

[56] Z. Ma, H. He, C. Deng, Y. Ren, D. Lu, W. Li, X. Sun, W. Wang, Y. Zhang, Y. Xu, X. Zhou, L. Zhou, J. Lin, T. Li, T. Wu, J. Wang, 3D bioprinting of proangiogenic constructs with induced immunomodulatory microenvironments through a dual cross-linking procedure using laponite incorporated bioink, Compos. B Eng. 229 (2022), 109399.

[57] P. Qiu, M. Li, K. Chen, B. Fang, P. Chen, Z. Tang, X. Lin, S. Fan, Periosteal matrix-derived hydrogel promotes bone repair through an early immune regulation coupled with enhanced angio- and osteogenesis, Biomaterials 227 (2020), 119552.

[58] Y. Zhai, K. Schilling, T. Wang, M. El Khatib, S. Vinogradov, E.B. Brown, X. Zhang, Spatiotemporal blood vessel specification at the osteogenesis and angiogenesis interface of biomimetic nanofiber-enabled bone tissue engineering, Biomaterials 276 (2021), 121041.

[59] M. Majidinia, J. Aghazadeh, R. Jahanban-Esfahlani, B. Yousefi, The roles of Wnt/β-catenin pathway in tissue development and regenerative medicine, J. Cell. Physiol. 233 (8) (2018) 5598–5612.

[60] X. Liu, W. Chen, B. Shao, X. Zhang, Y. Wang, S. Zhang, W. Wu, Mussel patterned with 4D biodegrading elastomer durably recruits regenerative macrophages to promote regeneration of craniofacial bone, Biomaterials 276 (2021), 120998.

[61] L. Chen, C. Deng, J. Li, Q. Yao, J. Chang, L. Wang, C. Wu, 3D printing of a lithium-calcium-silicate crystal bioscaffold with dual bioactivities for osteochondral interface reconstruction, Biomaterials 196 (2019) 138–150.

[62] M. Chen, Y. Zhang, W. Zhang, J. Li, Polyhedral oligomeric silsesquioxane-incorporated gelatin hydrogel promotes angiogenesis during vascularized bone regeneration, ACS Appl. Mater. Interfaces 12 (20) (2020) 22410–22425.

[63] L. Li, Q. Li, L. Gui, Y. Deng, L. Wang, J. Jiao, Y. Hu, X. Lan, J. Hou, Y. Li, D. Lu, Sequential gastrodin release PU/n-HA composite scaffolds reprogram macrophages for improved osteogenesis and angiogenesis, Bioact. Mater. 19 (2023) 24–37.